Measurement of CP-violating asymmetries in $B^0 \to (\rho\pi)^0$ decays using a time-dependent Dalitz plot analysis

J. P. Lees,[1] V. Poireau,[1] V. Tisserand,[1] E. Grauges,[2] A. Palano,[3a,3b] G. Eigen,[4] B. Stugu,[4] D. N. Brown,[5] L. T. Kerth,[5] Yu. G. Kolomensky,[5] G. Lynch,[5] H. Koch,[6] T. Schroeder,[6] D. J. Asgeirsson,[7] C. Hearty,[7] T. S. Mattison,[6] J. A. McKenna,[7] R. Y. So,[7] A. Khan,[8] V. E. Blinov,[9] A. R. Buzykaev,[9] V. P. Druzhinin,[9] V. B. Golubev,[9] E. A. Kravchenko,[9] A. P. Onuchin,[9] S. I. Serednyakov,[9] Yu. I. Skovpen,[9] E. P. Solodov,[9] K. Yu. Todyshev,[9] A. N. Yushkov,[9] D. Kirkby,[10] A. J. Lankford,[10] M. Mandelkern,[10] H. Atmacan,[11] J. W. Gary,[11] O. Long,[11] G. M. Vitug,[11] C. Campagnari,[12] T. M. Hong,[12] D. Kovalskyi,[12] J. D. Richman,[12] C. A. West,[12] A. M. Eisner,[13] J. Kroseberg,[13] W. S. Lockman,[13] A. J. Martinez,[13] B. A. Schumm,[13] A. Seiden,[13] D. S. Chao,[14] C. H. Cheng,[14] B. Echenard,[14] K. T. Flood,[14] D. G. Hitlin,[14] P. Ongmongkolkul,[14] F. C. Porter,[14] A. Y. Rakitin,[14] R. Andreassen,[15] Z. Huard,[15] B. T. Meadows,[15] M. D. Sokoloff,[15] L. Sun,[15] P. C. Bloom,[16] W. T. Ford,[16] A. Gaz,[16] U. Nauenberg,[16] J. G. Smith,[16] S. R. Wagner,[16] R. Ayad,[17,*] W. H. Toki,[17] B. Spaan,[18] K. R. Schubert,[19] R. Schwierz,[19] D. Bernard,[20] M. Verderi,[20] P. J. Clark,[21] S. Playfer,[21] D. Bettoni,[22a] C. Bozzi,[22a] R. Calabrese,[22a,22b] G. Cibinetto,[22a,22b] E. Fioravanti,[22a,22b] I. Garzia,[22a,22b] E. Luppi,[22a,22b] L. Piemontese,[22a] V. Santoro,[22a] R. Baldini-Ferroli,[23] A. Calcaterra,[23] R. de Sangro,[23] G. Finocchiaro,[23] P. Patteri,[23] I. M. Peruzzi,[23,†] M. Piccolo,[23] M. Rama,[23] A. Zallo,[23] R. Contri,[24a,24b] E. Guido,[24a,24b] M. Lo Vetere,[24a,24b] M. R. Monge,[24a,24b] S. Passaggio,[24a] C. Patrignani,[24a,24b] E. Robutti,[24a] B. Bhuyan,[25] V. Prasad,[25] M. Morii,[26] A. Adametz,[27] U. Uwer,[27] H. M. Lacker,[28] T. Lueck,[28] P. D. Dauncey,[29] U. Mallik,[30] C. Chen,[31] J. Cochran,[31] W. T. Meyer,[31] S. Prell,[31] A. E. Rubin,[31] A. V. Gritsan,[32] N. Arnaud,[33] M. Davier,[33] D. Derkach,[33] G. Grosdidier,[33] F. Le Diberder,[33] A. M. Lutz,[33] B. Malaescu,[33] P. Roudeau,[33] M. H. Schune,[33] A. Stocchi,[33] G. Wormser,[33] D. J. Lange,[34] D. M. Wright,[34] C. A. Chavez,[35] J. P. Coleman,[35] J. R. Fry,[35] E. Gabathuler,[35] D. E. Hutchcroft,[35] D. J. Payne,[35] C. Touramanis,[35] A. J. Bevan,[36] F. Di Lodovico,[36] R. Sacco,[36] M. Sigamani,[36] G. Cowan,[37] D. N. Brown,[38] C. L. Davis,[38] A. G. Denig,[39] M. Fritsch,[39] W. Gradl,[39] K. Griessinger,[39] A. Hafner,[39] E. Prencipe,[39] R. J. Barlow,[40,‡] G. Jackson,[40] G. D. Lafferty,[40] E. Behn,[41] R. Cenci,[41] B. Hamilton,[41] A. Jawahery,[41] D. A. Roberts,[41] C. Dallapiccola,[42] R. Cowan,[43] D. Dujmic,[43] G. Sciolla,[43] R. Cheaib,[44] D. Lindemann,[44] P. M. Patel,[44,§] S. H. Robertson,[44] P. Biassoni,[45a,45b] N. Neri,[45a] F. Palombo,[45a,45b] S. Stracka,[45a,45b] L. Cremaldi,[46] R. Godang,[46,‖] R. Kroeger,[46] P. Sonnek,[42] D. J. Summers,[46] X. Nguyen,[47] M. Simard,[47] P. Taras,[47] G. De Nardo,[48a,48b] D. Monorchio,[48a,48b] G. Onorato,[48a,48b] C. Sciacca,[48a,48b] M. Martinelli,[49] G. Raven,[49] C. P. Jessop,[50] J. M. LoSecco,[50] W. F. Wang,[50] K. Honscheid,[51] R. Kass,[51] J. Brau,[52] R. Frey,[52] N. B. Sinev,[52] D. Strom,[52] E. Torrence,[52] E. Feltresi,[53a,53b] N. Gagliardi,[53a,53b] M. Margoni,[53a,53b] M. Morandin,[53a] M. Posocco,[53a] M. Rotondo,[53a] G. Simi,[53a] F. Simonetto,[53a,53b] R. Stroili,[53a,53b] S. Akar,[54] E. Ben-Haim,[54] M. Bomben,[54] G. R. Bonneaud,[54] H. Briand,[54] G. Calderini,[54] J. Chauveau,[54] O. Hamon,[54] Ph. Leruste,[54] G. Marchiori,[54] J. Ocariz,[54] S. Sitt,[54] M. Biasini,[55a,55b] E. Manoni,[55a,55b] S. Pacetti,[55a,55b] A. Rossi,[55a,55b] C. Angelini,[56a,56b] G. Batignani,[56a,56b] S. Bettarini,[56a,56b] M. Carpinelli,[56a,56b,¶] G. Casarosa,[56a,56b] A. Cervelli,[56a,56b] F. Forti,[56a,56b] M. A. Giorgi,[56a,56b] A. Lusiani,[56a,56c] B. Oberhof,[56a,56b] A. Perez,[56a,56b] G. Rizzo,[56a,56b] J. J. Walsh,[56a] D. Lopes Pegna,[57] J. Olsen,[57] A. J. S. Smith,[57] F. Anulli,[58a] R. Faccini,[58a,58b] F. Ferrarotto,[58a] F. Ferroni,[58a,58b] M. Gaspero,[58a,58b] L. Li Gioi,[58a] M. A. Mazzoni,[58a] G. Piredda,[58a] C. Bünger,[59] O. Grünberg,[59] T. Hartmann,[59] T. Leddig,[59] C. Voß,[59] R. Waldi,[59] T. Adye,[60] E. O. Olaiya,[60] F. F. Wilson,[60] S. Emery,[61] G. Hamel de Monchenault,[61] G. Vasseur,[61] Ch. Yèche,[61] D. Aston,[62] R. Bartoldus,[62] J. F. Benitez,[62] C. Cartaro,[62] M. R. Convery,[62] J. Dorfan,[62] G. P. Dubois-Felsmann,[62] W. Dunwoodie,[62] M. Ebert,[62] R. C. Field,[62] M. Franco Sevilla,[62] B. G. Fulsom,[62] A. M. Gabareen,[62] M. T. Graham,[62] P. Grenier,[62] C. Hast,[62] W. R. Innes,[62] M. H. Kelsey,[62] P. Kim,[62] M. L. Kocian,[62] D. W. G. S. Leith,[62] P. Lewis,[62] B. Lindquist,[62] S. Luitz,[62] V. Luth,[62] H. L. Lynch,[62] D. B. MacFarlane,[62] D. R. Muller,[62] H. Neal,[62] S. Nelson,[62] M. Perl,[62] T. Pulliam,[62] B. N. Ratcliff,[62] A. Roodman,[62] A. A. Salnikov,[62] R. H. Schindler,[62] A. Snyder,[62] D. Su,[62] M. K. Sullivan,[62] J. Va'vra,[62] A. P. Wagner,[62] W. J. Wisniewski,[62] M. Wittgen,[62] D. H. Wright,[62] H. W. Wulsin,[62] C. C. Young,[62] V. Ziegler,[62] W. Park,[63] M. V. Purohit,[63] R. M. White,[63] J. R. Wilson,[63] A. Randle-Conde,[64] S. J. Sekula,[64] M. Bellis,[65] P. R. Burchat,[65] T. S. Miyashita,[65] E. M. T. Puccio,[65] M. S. Alam,[66] J. A. Ernst,[66] R. Gorodeisky,[67] N. Guttman,[67] D. R. Peimer,[67] A. Soffer,[67] S. M. Spanier,[68] J. L. Ritchie,[69] A. M. Ruland,[69] R. F. Schwitters,[69] B. C. Wray,[69] J. M. Izen,[70] X. C. Lou,[70] F. Bianchi,[71a,71b] D. Gamba,[71a,71b] S. Zambito,[71a,71b] L. Lanceri,[72a,72b] L. Vitale,[72a,72b] F. Martinez-Vidal,[73] A. Oyanguren,[73] P. Villanueva-Perez,[73] H. Ahmed,[74] J. Albert,[74] Sw. Banerjee,[74] F. U. Bernlochner,[74] H. H. F. Choi,[74] G. J. King,[74] R. Kowalewski,[74] M. J. Lewczuk,[74] I. M. Nugent,[74] J. M. Roney,[74] R. J. Sobie,[74] N. Tasneem,[74] T. J. Gershon,[75] P. F. Harrison,[75] T. E. Latham,[75] H. R. Band,[75] S. Dasu,[76] Y. Pan,[76] R. Prepost,[76] and S. L. Wu[76]

(*BABAR* Collaboration)

[1]*Laboratoire d'Annecy-le-Vieux de Physique des Particules (LAPP), Université de Savoie, CNRS/IN2P3, F-74941 Annecy-Le-Vieux, France*
[2]*Universitat de Barcelona, Facultat de Fisica, Departament ECM, E-08028 Barcelona, Spain*
[3a]*INFN Sezione di Bari, I-70126 Bari, Italy*
[3b]*Dipartimento di Fisica, Università di Bari, I-70126 Bari, Italy*
[4]*University of Bergen, Institute of Physics, N-5007 Bergen, Norway*
[5]*Lawrence Berkeley National Laboratory and University of California, Berkeley, California 94720, USA*
[6]*Ruhr Universität Bochum, Institut für Experimentalphysik 1, D-44780 Bochum, Germany*
[7]*University of British Columbia, Vancouver, British Columbia, Canada V6T 1Z1*
[8]*Brunel University, Uxbridge, Middlesex UB8 3PH, United Kingdom*
[9]*Budker Institute of Nuclear Physics, Novosibirsk 630090, Russia*
[10]*University of California at Irvine, Irvine, California 92697, USA*
[11]*University of California at Riverside, Riverside, California 92521, USA*
[12]*University of California at Santa Barbara, Santa Barbara, California 93106, USA*
[13]*University of California at Santa Cruz, Institute for Particle Physics, Santa Cruz, California 95064, USA*
[14]*California Institute of Technology, Pasadena, California 91125, USA*
[15]*University of Cincinnati, Cincinnati, Ohio 45221, USA*
[16]*University of Colorado, Boulder, Colorado 80309, USA*
[17]*Colorado State University, Fort Collins, Colorado 80523, USA*
[18]*Technische Universität Dortmund, Fakultät Physik, D-44221 Dortmund, Germany*
[19]*Technische Universität Dresden, Institut für Kern- und Teilchenphysik, D-01062 Dresden, Germany*
[20]*Laboratoire Leprince-Ringuet, Ecole Polytechnique, CNRS/IN2P3, F-91128 Palaiseau, France*
[21]*University of Edinburgh, Edinburgh EH9 3JZ, United Kingdom*
[22a]*INFN Sezione di Ferrara, I-44100 Ferrara, Italy*
[22b]*Dipartimento di Fisica, Università di Ferrara, I-44100 Ferrara, Italy*
[23]*INFN Laboratori Nazionali di Frascati, I-00044 Frascati, Italy*
[24a]*INFN Sezione di Genova, I-16146 Genova, Italy*
[24b]*Dipartimento di Fisica, Università di Genova, I-16146 Genova, Italy*
[25]*Indian Institute of Technology Guwahati, Guwahati, Assam 781 039, India*
[26]*Harvard University, Cambridge, Massachusetts 02138, USA*
[27]*Universität Heidelberg, Physikalisches Institut, Philosophenweg 12, D-69120 Heidelberg, Germany*
[28]*Humboldt-Universität zu Berlin, Institut für Physik, Newtonstraße 15, D-12489 Berlin, Germany*
[29]*Imperial College London, London SW7 2AZ, United Kingdom*
[30]*University of Iowa, Iowa City, Iowa 52242, USA*
[31]*Iowa State University, Ames, Iowa 50011-3160, USA*
[32]*Johns Hopkins University, Baltimore, Maryland 21218, USA*
[33]*Laboratoire de l'Accélérateur Linéaire, IN2P3/CNRS et Université Paris-Sud 11, Centre Scientifique d'Orsay, F-91898 Orsay Cedex, France*
[34]*Lawrence Livermore National Laboratory, Livermore, California 94550, USA*
[35]*University of Liverpool, Liverpool L69 7ZE, United Kingdom*
[36]*Queen Mary, University of London, London E1 4NS, United Kingdom*
[37]*University of London, Royal Holloway and Bedford New College, Egham, Surrey TW20 0EX, United Kingdom*
[38]*University of Louisville, Louisville, Kentucky 40292, USA*
[39]*Johannes Gutenberg-Universität Mainz, Institut für Kernphysik, D-55099 Mainz, Germany*
[40]*University of Manchester, Manchester M13 9PL, United Kingdom*
[41]*University of Maryland, College Park, Maryland 20742, USA*
[42]*University of Massachusetts, Amherst, Massachusetts 01003, USA*
[43]*Massachusetts Institute of Technology, Laboratory for Nuclear Science, Cambridge, Massachusetts 02139, USA*
[44]*McGill University, Montréal, Québec, Canada H3A 2T8*
[45a]*INFN Sezione di Milano, I-20133 Milano, Italy*
[45b]*Dipartimento di Fisica, Università di Milano, I-20133 Milano, Italy*
[46]*University of Mississippi, University, Mississippi 38677, USA*
[47]*Université de Montréal, Physique des Particules, Montréal, Québec, Canada H3C 3J7*
[48a]*INFN Sezione di Napoli, I-80126 Napoli, Italy*
[48b]*Dipartimento di Scienze Fisiche, Università di Napoli Federico II, I-80126 Napoli, Italy*
[49]*NIKHEF, National Institute for Nuclear Physics and High Energy Physics, NL-1009 DB Amsterdam, The Netherlands*
[50]*University of Notre Dame, Notre Dame, Indiana 46556, USA*
[51]*Ohio State University, Columbus, Ohio 43210, USA*
[52]*University of Oregon, Eugene, Oregon 97403, USA*
[53a]*INFN Sezione di Padova, I-35131 Padova, Italy*
[53b]*Dipartimento di Fisica, Università di Padova, I-35131 Padova, Italy*

[54]*Laboratoire de Physique Nucléaire et de Hautes Energies, IN2P3/CNRS, Université Pierre et Marie Curie-Paris6, Université Denis Diderot-Paris7, F-75252 Paris, France*
[55a]*INFN Sezione di Perugia, I-06100 Perugia, Italy*
[55b]*Dipartimento di Fisica, Università di Perugia, I-06100 Perugia, Italy*
[56a]*INFN Sezione di Pisa, I-56127 Pisa, Italy*
[56b]*Dipartimento di Fisica, Università di Pisa, I-56127 Pisa, Italy*
[56c]*Scuola Normale Superiore di Pisa, I-56127 Pisa, Italy*
[57]*Princeton University, Princeton, New Jersey 08544, USA*
[58a]*INFN Sezione di Roma, I-00185 Roma, Italy*
[58b]*Dipartimento di Fisica, Università di Roma La Sapienza, I-00185 Roma, Italy*
[59]*Universität Rostock, D-18051 Rostock, Germany*
[60]*Rutherford Appleton Laboratory, Chilton, Didcot, Oxon OX11 0QX, United Kingdom*
[61]*CEA, Irfu, SPP, Centre de Saclay, F-91191 Gif-sur-Yvette, France*
[62]*SLAC National Accelerator Laboratory, Stanford, California 94309 USA*
[63]*University of South Carolina, Columbia, South Carolina 29208, USA*
[64]*Southern Methodist University, Dallas, Texas 75275, USA*
[65]*Stanford University, Stanford, California 94305-4060, USA*
[66]*State University of New York, Albany, New York 12222, USA*
[67]*Tel Aviv University, School of Physics and Astronomy, Tel Aviv 69978, Israel*
[68]*University of Tennessee, Knoxville, Tennessee 37996, USA*
[69]*University of Texas at Austin, Austin, Texas 78712, USA*
[70]*University of Texas at Dallas, Richardson, Texas 75083, USA*
[71a]*INFN Sezione di Torino, I-10125 Torino, Italy*
[71b]*Dipartimento di Fisica Sperimentale, Università di Torino, I-10125 Torino, Italy*
[72a]*INFN Sezione di Trieste, I-34127 Trieste, Italy*
[72b]*Dipartimento di Fisica, Università di Trieste, I-34127 Trieste, Italy*
[73]*IFIC, Universitat de Valencia-CSIC, E-46071 Valencia, Spain*
[74]*University of Victoria, Victoria, British Columbia, Canada V8W 3P6*
[75]*Department of Physics, University of Warwick, Coventry CV4 7AL, United Kingdom*
[76]*University of Wisconsin, Madison, Wisconsin 53706, USA*
(Received 15 April 2013; published 19 July 2013)

We present results for a time-dependent Dalitz plot measurement of *CP*-violating asymmetries in the mode $B^0 \to \pi^+\pi^-\pi^0$. The data set is derived from the complete sample of 471×10^6 $B\bar{B}$ meson pairs collected with the *BABAR* detector at the PEP-II asymmetric-energy e^+e^- collider at the SLAC National Accelerator Laboratory operating on the $\Upsilon(4S)$ resonance. We extract parameters describing the time-dependent $B^0 \to \rho\pi$ decay probabilities and *CP* asymmetries, including $\mathcal{C} = 0.016 \pm 0.059 \pm 0.036$, $\Delta\mathcal{C} = 0.234 \pm 0.061 \pm 0.048$, $\mathcal{S} = 0.053 \pm 0.081 \pm 0.034$, and $\Delta\mathcal{S} = 0.054 \pm 0.082 \pm 0.039$, where the uncertainties are statistical and systematic, respectively. We perform a two-dimensional likelihood scan of the direct *CP*-violation asymmetry parameters for $B^0 \to \rho^\pm\pi^\mp$ decays, finding the change in χ^2 between the minimum and the origin (corresponding to no direct *CP* violation) to be $\Delta\chi^2 = 6.42$. We present information on the *CP*-violating parameter α in a likelihood scan that incorporates $B^\pm \to \rho\pi$ measurements. To aid in the interpretation of our results, statistical robustness studies are performed to assess the reliability with which the true values of the physics parameters can be extracted. Significantly, these studies indicate that α cannot be reliably extracted with our current sample size, though the other physics parameters are robustly extracted.

DOI: 10.1103/PhysRevD.88.012003 PACS numbers: 11.30.Er, 12.15.Ff

I. INTRODUCTION

Within the standard model (SM) of particle physics, *CP* violation in the quark sector is described by the Cabibbo-Kobayashi-Maskawa (CKM) quark-mixing matrix. Physics beyond the SM may result in measured values of observables that deviate from the values expected based on other CKM parameter measurements and the SM.

The decay $B^0 \to \pi^+\pi^-\pi^0$ [1] is well suited to the study of *CP* violation and has been previously explored by both

*Present address: University of Tabuk, Tabuk 71491, Saudi Arabia.
†Also at Università di Perugia, Dipartimento di Fisica, Perugia, Italy.
‡Present address: University of Huddersfield, Huddersfield HD1 3DH, United Kingdom.
§Deceased.
‖Present address: University of South Alabama, Mobile, Alabama 36688, USA.
¶Also at Università di Sassari, Sassari, Italy.

the *BABAR* [2] and Belle [3] Collaborations. Early studies of this mode were "quasi-two-body" (Q2B) analyses that treated each ρ resonance separately in the decays $B^0 \to \rho^0\pi^0(\rho^0 \to \pi^+\pi^-)$ and $B^0 \to \rho^\pm\pi^\mp(\rho^\pm \to \pi^\pm\pi^0)$. However, as first noted by Snyder and Quinn [4], a complete time-dependent Dalitz plot (DP) analysis is sensitive to the interference between the strong and weak amplitudes in the regions where the ρ^+, ρ^-, and ρ^0 resonances overlap. This interference allows the unambiguous extraction of the strong and weak relative phases, and of the CP-violating parameter $\alpha \equiv \arg[-V_{td}V_{tb}^*/(V_{ud}V_{ub}^*)]$, where $V_{qq'}$ are components of the CKM matrix. A precision measurement of α is of interest because it serves to further test the SM and constrain new physics that may contribute to loops in Feynman diagrams.

In this paper, we present an update of an earlier *BABAR* analysis. We use the full *BABAR* data set collected at the $\Upsilon(4S)$ resonance, corresponding to an increase of 25% in the number of B meson decays, and include a number of improvements to both the reconstruction and selection procedures. Among these are improved charged-particle tracking and particle identification (PID), and a reoptimized multivariate discriminator, used both for event selection and as a variable in the final fit.

Another new feature of this analysis is a series of studies of the statistical robustness with which the true values of physics parameters can be extracted. These studies, described in an appendix, reveal that α cannot be reliably extracted with our current sample size, though the other physics parameters are robustly extracted.

Section II contains an introduction to the theory behind this analysis and the formalism used. We proceed to descriptions of the detector (Sec. III), the data sets (Sec. IV), and the event selection procedures (Sec. V). This is followed by a presentation of the fitting procedure (Sec. VI) and of the systematic studies (Sec. VII). Finally, we present the fit results (Sec. VIII) and a conclusion (Sec. IX). An overview of robustness studies is provided in an Appendix.

II. THEORY OVERVIEW

A. Time-independent probability distribution

The time-independent amplitudes for B^0 and $\bar{B}^0$ decays to $\pi^+\pi^-\pi^0$ are given by

$$\begin{aligned} A_{3\pi} &= f_+A^+ + f_-A^- + f_0A^0, \\ \bar{A}_{3\pi} &= f_+\bar{A}^+ + f_-\bar{A}^- + f_0\bar{A}^0, \end{aligned} \tag{1}$$

respectively, where A^κ and $\bar{A}^\kappa$ with $\kappa \in \{+,-,0\}$ are complex amplitudes associated with the ρ^+, ρ^-, and ρ^0 resonances, respectively, and $f_\kappa = f_\kappa(m,\theta_\kappa)$ are defined in terms of modified relativistic Breit-Wigner resonances [5] modeling the three ρ resonances. The angle θ_κ is the helicity angle for the resonance, defined as the angle between the π^0 (π^-) momentum and the negative of the momentum of the recoiling π^- (π^+) for the ρ^+ (ρ^-), and as the angle between the π^+ momentum and the negative of the momentum of the recoiling π^0 for the ρ^0. All helicity angles are calculated in the ρ rest frame. In the fit, we include the $\rho(770)$ as well as its radial excitation, the $\rho(1450)$; therefore, each f_κ is a sum of modified relativistic Breit-Wigner resonances, F, for the $\rho^\kappa(770)$ and $\rho^\kappa(1450)$,

$$f_\kappa(m,\theta_\kappa) \propto F_{\rho(770)}(m,\theta_\kappa) + a_{\rho'}e^{i\phi_{\rho'}}F_{\rho(1450)}(m,\theta_\kappa), \tag{2}$$

where $a_{\rho'}$ and $\phi_{\rho'}$ are the magnitude and phase of the $\rho(1450)$ resonance relative to the $\rho(770)$. We include systematic uncertainties, described in Sec. VII A, to account for possible contributions from the $\rho(1700)$.

B. Time-dependent probability distribution

Using the time-independent amplitudes $A_{3\pi}$ and $\bar{A}_{3\pi}$, we can express the full time-dependent probability for a meson that is a B^0 ($\mathcal{A}_{3\pi}^-$) or $\bar{B}^0$ ($\mathcal{A}_{3\pi}^+$) at the time the other B meson decays, to decay to $\pi^+\pi^-\pi^0$ as

$$\begin{aligned} |\mathcal{A}_{3\pi}^\pm(\Delta t)|^2 = \frac{e^{-|\Delta t|/\tau_{B^0}}}{4\tau_{B^0}}\Big(&|A_{3\pi}|^2 + |\bar{A}_{3\pi}|^2 \\ &\mp (|A_{3\pi}|^2 - |\bar{A}_{3\pi}|^2)\cos(\Delta m_d\Delta t) \\ &\pm 2\,\mathrm{Im}\Big[\frac{q}{p}\bar{A}_{3\pi}A_{3\pi}^*\Big]\sin(\Delta m_d\Delta t)\Big), \end{aligned} \tag{3}$$

where τ_{B^0} is the mean neutral B lifetime, Δm_d is the mass difference between the heavy and light neutral B mass eigenstates, p and q are the complex parameters in the definitions of the neutral mass eigenstates $p|B^0\rangle \pm q|\bar{B}^0\rangle$, and Δt is the time difference between the decays of the fully reconstructed B meson ($B_{3\pi}$) and the B meson used to determine the B flavor (B_{tag}). In Eq. (3), as in the fit, we assume that the heavy and light mass eigenstates have the same lifetime, that there is no CP violation in $B^0\bar{B}^0$ mixing ($|q/p| = 1$), and that CPT is conserved.

C. Square Dalitz plot formalism

While nonresonant phase-space decays uniformly populate the kinematically allowed region of a DP, signal $\rho\pi$ events populate the boundaries of this region due to the low mass of the ρ resonances relative to the B mass. In particular, the interference regions of the signal DP, which provide sensitivity to the relative phases of the ρ resonances, are confined to small regions in the three corners of the DP. In order to expand these regions of interest and avoid the use of bins of variable size, we perform a transformation of the DP that maps the kinematically allowed region onto a dimensionless unit square. The transformation is described by

$$dm_+dm_- \to |\det J|dm'd\theta', \tag{4}$$

with the square Dalitz plot (SDP) coordinates,

$$m' \equiv \frac{1}{\pi}\arccos\left(2\frac{m_0 - m_0^{\min}}{m_0^{\max} - m_0^{\min}} - 1\right), \tag{5}$$

$$\theta' \equiv \frac{1}{\pi}\theta_0, \tag{6}$$

where $m_\pm$ is the invariant mass of the $\pi^\pm\pi^0$ system, m_0 is the invariant mass of the two charged pion candidates, θ_0 is the ρ^0 helicity angle defined earlier, $m_0^{\max} = m_{B^0} - m_{\pi^0}$ and $m_0^{\min} = 2m_{\pi^+}$ are the kinematic limits of the m_0 mass, and J is the Jacobian of the transformation. The determinant of the Jacobian is given by

$$|\det J| = 4|\mathbf{p}_+^*||\mathbf{p}_0^*|m_0\frac{\partial m_0}{\partial m'}\frac{\partial\cos\theta_0}{\partial\theta'}, \tag{7}$$

where

$$|\mathbf{p}_+^*| = \sqrt{(E_+^*)^2 - m_{\pi^+}^2}, \tag{8}$$

$$|\mathbf{p}_0^*| = \sqrt{(E_0^*)^2 - m_{\pi^0}^2}, \tag{9}$$

and the energies E_+^* and E_0^* of the π^+ and π^0 are defined in the $\pi^+\pi^-$ center-of-mass (CM) frame. Figure 1 shows an example of a standard DP (left) and its transformed SDP counterpart (right), plotted using simulated $B^0 \to \rho\pi$ decays, where the three ρ resonances are assumed to have the same amplitude.

D. U/I formalism

If one explicitly inserts Eq. (1) into Eq. (3), the full time-dependent amplitude for a B^0 or $\bar{B}^0$ meson to decay to $\pi^+\pi^-\pi^0$ can be written in terms of

$$|\mathcal{A}_{3\pi}|^2 \pm |\bar{\mathcal{A}}_{3\pi}|^2 = \sum_{\kappa\in[+,-,0]}|f_\kappa|^2 U_\kappa^\pm + 2\sum_{\kappa<\sigma\in[+,-,0]}(\mathrm{Re}[f_\kappa f_\sigma^*]U_{\kappa\sigma}^{\pm,\mathrm{Re}} - \mathrm{Im}[f_\kappa f_\sigma^*]U_{\kappa\sigma}^{\pm,\mathrm{Im}}), \tag{10}$$

and

$$\mathrm{Im}\left[\frac{q}{p}\bar{\mathcal{A}}_{3\pi}\mathcal{A}_{3\pi}^*\right] = \sum_{\kappa\in[+,-,0]}|f_\kappa|^2 I_\kappa + \sum_{\kappa<\sigma\in[+,-,0]}(\mathrm{Re}[f_\kappa f_\sigma^*]I_{\kappa\sigma}^{\mathrm{Im}} + \mathrm{Im}[f_\kappa f_\sigma^*]I_{\kappa\sigma}^{\mathrm{Re}}), \tag{11}$$

with

$$U_\kappa^\pm = |A^\kappa|^2 \pm |\bar{A}^\kappa|^2, \tag{12}$$

$$U_{\kappa\sigma}^{\pm,\mathrm{Re(Im)}} = \mathrm{Re(Im)}[A^\kappa A^{\sigma*} \pm \bar{A}^\kappa\bar{A}^{\sigma*}], \tag{13}$$

$$I_\kappa = \mathrm{Im}[\bar{A}^\kappa A^{\kappa*}], \tag{14}$$

$$I_{\kappa\sigma}^{\mathrm{Re}} = \mathrm{Re}[\bar{A}^\kappa A^{\sigma*} - \bar{A}^\sigma A^{\kappa*}], \tag{15}$$

$$I_{\kappa\sigma}^{\mathrm{Im}} = \mathrm{Im}[\bar{A}^\kappa A^{\sigma*} + \bar{A}^\sigma A^{\kappa*}]. \tag{16}$$

The 27 real-valued U and I coefficients provide an alternative parametrization to tree and penguin amplitudes (as well as α) or to the amplitudes A^κ and $\bar{A}^\kappa$ [6]. The U and I parameters can also be directly related to the Q2B $\mathcal{C}$ and $\mathcal{S}$ parameters often used in *CP*-violation analyses [7], where $\mathcal{C}$ parametrizes direct *CP* violation, and $\mathcal{S}$ parametrizes mixing-induced *CP* violation (involving the angle α in this analysis). The related parameter $\Delta\mathcal{C}$ describes the asymmetry between the rates $\Gamma(B^0 \to \rho^+\pi^-) + \Gamma(\bar{B}^0 \to \rho^-\pi^+)$ and $\Gamma(B^0 \to \rho^-\pi^+) + \Gamma(\bar{B}^0 \to \rho^+\pi^-)$,

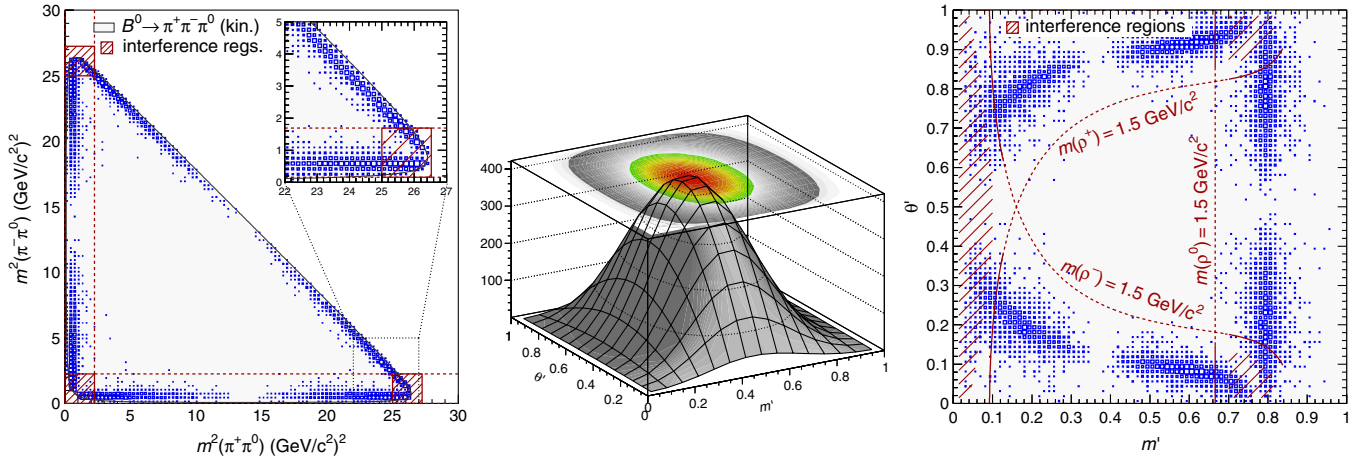

FIG. 1 (color online). Nominal (left) and square (right) $B^0 \to \rho\pi$ Dalitz plots obtained from Monte Carlo generated events without detector simulation [2]. The amplitudes in Eq. (1) are generated with values $A^+ = A^- = A^0 = 1$ so that they interfere destructively for equal $\pi\pi$ masses. The hatched areas indicate the main overlap regions between the different ρ bands. The dashed lines in the square Dalitz plot correspond to $m(\rho^{+,-,0}) = 1.5$ GeV$/c^2$. The middle plot depicts the Jacobian determinant of the transformation and shows the distribution in the square Dalitz plot for uniformly distributed events in the nominal Dalitz plot.

while $\Delta\mathcal{S}$ is related to the strong phase difference between the different amplitudes describing the decay $B^0 \to \rho\pi$. The U and I parameters are related to the $\mathcal{C}$ and $\mathcal{S}$ parameters through the relations

$$\mathcal{C}^+ = \frac{U_+^-}{U_+^+}, \quad \mathcal{C}^- = \frac{U_-^-}{U_-^+}, \quad \mathcal{S}^+ = \frac{2I_+}{U_+^+}, \quad \mathcal{S}^- = \frac{2I_-}{U_-^+}, \quad (17)$$

and

$$\mathcal{A}_{\rho\pi} = \frac{U_+^+ - U_-^+}{U_+^+ + U_-^+}, \quad (18)$$

where

$$\mathcal{C} = (\mathcal{C}^+ + \mathcal{C}^-)/2, \quad (19)$$

$$\Delta\mathcal{C} = (\mathcal{C}^+ - \mathcal{C}^-)/2, \quad (20)$$

$$\mathcal{S} = (\mathcal{S}^+ + \mathcal{S}^-)/2, \quad (21)$$

$$\Delta\mathcal{S} = (\mathcal{S}^+ - \mathcal{S}^-)/2. \quad (22)$$

Note that while $\mathcal{C}$, $\mathcal{S}$, $\Delta\mathcal{C}$, and $\Delta\mathcal{S}$ do not depend on interference effects between the ρ resonances, the U and I parameter formalism accounts for these features and is thus appropriate for a full DP analysis. While some degree of physical intuition is lost when using the U and I parameters instead of the standard complex amplitudes and phases, there are several practical motivating factors for their adoption in the fit:

(i) Whereas there is a twofold ambiguity in α (α versus $90° - \alpha$), there is a unique solution in a fit to the U and I parameters, which encompasses both solutions for α).

(ii) The U and I parametrization results in uncertainties that are more Gaussian than those in a standard amplitude and phase fit.

(iii) It is simpler to average U and I fit results from different measurements or experiments that publish the full covariance matrix.

For physical solutions, there are constraints between the U and I parameters. In the case of three ρ resonances (ρ^+, ρ^-, and ρ^0), a fit to the complex tree and penguin amplitudes as well as the weak phase α involves 11 unknown parameters, which reduce to 10 parameters when the arbitrary global phase is removed. A U and I fit is equivalent to such a fit, but involves many more parameters. However, when the $\rho^0\pi^0$ amplitude is small, as is observed in nature, the values of 11 of the 27 U and I parameters become unimportant. Due to the high degree of correlation between the various U and I fit parameters, the 27 parameters actually represent only 12 independent parameters. Neglecting the arbitrary phase and the overall normalization, this reduces to 10, and once isospin relations are taken into account, only 9 independent parameters remain.

Because the U and I formalism is used in the final fit without any constraints on the parameters (aside from fixing $U_+^+ = 1$ to set the overall normalization), it is possible for the free parameters to take on unphysical values that do not correspond to any physical set of ρ amplitudes. The final fit values from the 2007 *BABAR* analysis [2] are one such unphysical set. We determined that no biases are introduced due to the fitted values of the parameters being unphysical.

III. THE *BABAR* DETECTOR AND EXPERIMENT

The data used in this analysis were collected with the *BABAR* detector at the PEP-II asymmetric-energy e^+e^- storage ring at SLAC. A detailed description of the *BABAR* detector is presented in Ref. [8]. The tracking system used for track and vertex reconstruction has two components: a 5-layer silicon vertex tracker and a drift chamber, both operating within a 1.5 T magnetic field generated by a superconducting solenoidal magnet. A detector of internally reflected Cherenkov light associates Cherenkov photons with tracks for particle identification. The energies of photons and electrons are determined from the measured light produced in electromagnetic showers inside a CsI(Tl) crystal electromagnetic calorimeter. Muon candidates are identified with the use of the instrumented flux return of the solenoid. The flux return instrumentation initially consisted of resistive plate chambers and was later modified to consist of a mixture of resistive plate chambers and limited streamer tubes.

IV. DATA SAMPLE AND MC SIMULATION

A. Data samples

For the final fit, we use the full "on-resonance" *BABAR* data set of 431.0 fb^{-1} [9] collected at the $\Upsilon(4S)$ resonance energy ($\sqrt{s} = 10.58$ GeV/c^2). When optimizing background suppression criteria, 44.6 fb^{-1} of "off-resonance" data, collected 40 MeV below the $\Upsilon(4S)$ resonance, are used to model "continuum" $e^+e^- \to q\bar{q}$ ($q = u, d, s, c$) background.

B. Monte Carlo samples

Event simulation based on the Monte Carlo (MC) method is used to evaluate backgrounds and to determine signal-event reconstruction efficiencies. For all MC samples, detector response is accounted for using the GEANT4 package [10] in a full *BABAR* detector simulation.

$B^0 \to \rho^+\pi^-$ and $B^0 \to \rho^0\pi^0$ signal decays are simulated in separate MC data sets, but the $B^0 \to \rho^0\pi^0$ sample is not used to determine background selection criteria or to model signal distributions since the nominal branching fraction for $B^0 \to \rho^\pm\pi^\mp$ is 11.5 ± 3.1 times larger than the branching fraction for $B^0 \to \rho^0\pi^0$ [11].

B-decay backgrounds are modeled using MC samples consisting of B decays to specific final states as well as "generic" MC samples consisting of charged and neutral B decays to unconstrained final states. In the generic MC, dominant branching fractions are fixed to the results of

recent measurements [12]. Due to the uncertainty on branching fractions for charmless decays, all charmless events are removed from the generic MC and charmless modes of interest are explicitly included among the B background samples consisting of decays to specific final states. We use a total of 24 B-decay MC samples corresponding to 29 different final states (Table I) as well as MC samples of generic charged and neutral B decays.

The expected number of events for each charmless B background is calculated according to

$$n_{\rm exp} = 2n_{B\bar{B}}\mathcal{B}\mathcal{B}_{\rm mode}\epsilon, \tag{23}$$

where $n_{B\bar{B}}$ is the number of produced $B\bar{B}$ pairs, $\mathcal{B}$ is the branching fraction [12] (approximately $1/2$) for an $\Upsilon(4S)$ to decay to a charged or neutral $B\bar{B}$ pair (whichever is appropriate for the mode in question), $\mathcal{B}_{\rm mode}$ is the branching fraction for the B decay mode, and ϵ is the efficiency for reconstructing events in the mode, determined from MC. The factor of 2 is included because either of the B mesons in a given event may decay to the mode of interest.

In the case of the charged and neutral generic B backgrounds, the number of events expected for each mode is

$$n_{\rm exp} = n_{\rm MC}\frac{n_{B\bar{B}}\mathcal{B}}{n_{\rm gen}}, \tag{24}$$

where $n_{\rm gen}$ is the number of generated charged (neutral) MC events and $n_{\rm MC}$ is the number of charged (neutral) generic MC events that remain after all selection criteria have been applied.

An additional simulated data set, which is used for validation studies, consists of DP-parametrized $B^0 \to \rho\pi$ decays. This data set is used to verify flavor-tagging conventions.

V. EVENT SELECTION AND BACKGROUND SUPPRESSION

A. Event preselection

The kinematics of B meson decays that are fully reconstructed at *BABAR* can be characterized by two variables:

TABLE I. B background decay modes included in the final fit. Modes generated taking into account interference effects in the Dalitz plot are indicated by the "Dalitz" label. Longitudinal polarization is indicated by "[longitudinal]."

Class	Decay mode	$\mathcal{B}$ [10^{-6}]	# of expected events
0	$B^+ \to \rho^+\rho^0$ [longitudinal]	24.0 ± 1.9	129 ± 10
0	$B^+ \to a_1^+(\to (\rho\pi)^+)\pi^0$	26 ± 7	53 ± 14
0	$B^+ \to a_1^0(\to \rho^\pm\pi^\mp)\pi^+$	20 ± 6	37 ± 11
1	$B^+ \to \pi^+ K_s^0(\to \pi^+\pi^-)$	7.99 ± 0.35	6.96 ± 0.31
2	$B^+ \to K^+\pi^+\pi^-$ Dalitz	51.0 ± 2.9	34.8 ± 2.0
2	$B^+ \to \pi^+\pi^+\pi^-$ Dalitz	16.2 ± 1.5	203 ± 19
3	$B^+ \to \pi^0\rho^+$	10.9 ± 1.4	120 ± 15
3	$B^+ \to \pi^+ K_s^0(\to \pi^0\pi^0)$	3.54 ± 0.15	24.2 ± 1.1
4	$B^+ \to \pi^+\pi^0$	5.7 ± 0.5	38.6 ± 3.4
4	$B^+ \to K^+\pi^0$	12.9 ± 0.6	18.6 ± 0.9
5	$B^0 \to K_s^0\pi^+\pi^-$ Dalitz	44.8 ± 2.6	15.7 ± 0.9
6	$B^0 \to \rho^+\rho^-$ [longitudinal]	24.2 ± 3.1	122 ± 16
6	$B^0 \to a_1^-\pi^+$	33 ± 5	61 ± 9
6	$B^0 \to a_1^0\pi^0$	11.0 ± 1.7	22.8 ± 3.5
7	$B^0 \to K^+\pi^-$	19.4 ± 0.6	21.6 ± 0.7
8	$B^0 \to K^+\pi^-\pi^0$ Dalitz	35.9 ± 2.6	398 ± 29
9	$B^0 \to \gamma K^{*0}(892)(\to K^+\pi^-)$	40.1 ± 2.0	31.8 ± 1.6
9	$B^0 \to \gamma K^{*0}(1430)(\to K^+\pi^-)$	12.4 ± 2.4	3.2 ± 0.6
9	$B^0 \to \eta'(\to \rho^0\gamma)\pi^0$	0.35 ± 0.18	4.2 ± 2.1
10	$B^0 \to \pi^0 K_s^0(\to \pi^+\pi^-)$	3.39 ± 0.21	21.8 ± 1.4
11	$B^0 \to D^-(\to \pi^-\pi^0)\pi^+$	3.35 ± 0.27	399 ± 32
12	$B^0 \to \bar{D}^0(\to K^+\pi^-, K^+\pi^-\pi^0)\pi^0$	46.7 ± 4.5	124 ± 12
13	$B^0 \to \bar{D}^0(\to \pi^+\pi^-)\pi^0$	0.367 ± 0.034	48 ± 5
14	$B^0 \to J/\psi(\to e^+e^-, \mu^+\mu^-)\pi^0$	2.09 ± 0.19	153 ± 14
15	$B^0 \to$ neutral generic $b \to c$ decays		466 ± 14
16	$B^+ \to$ charged generic $b \to c$ decays		921 ± 21
	Total		3478 ± 65

$m_{\rm ES}$ and ΔE. The beam-energy-substituted mass $m_{\rm ES}$ is the invariant mass of the reconstructed B candidate calculated under the assumption that its energy in the e^+e^- CM frame is half the total beam energy. We define

$$m_{\rm ES} = \sqrt{[(s/2 + \vec{p}_i \cdot \vec{p}_B)/E_i]^2 - |\vec{p}_B|^2}, \qquad (25)$$

where $\sqrt{s}$ is the total beam energy in the e^+e^- CM frame, $(E_i, \vec{p}_i)$ is the four-momentum of the e^+e^- system in the laboratory frame, and $\vec{p}_B$ is the B-candidate momentum in the laboratory frame. The second kinematic variable is defined by

$$\Delta E = E_B^* - \frac{1}{2}\sqrt{s}, \qquad (26)$$

where E_B^* is the measured energy of the B candidate in the e^+e^- CM frame.

Pairs of oppositely charged tracks are combined with $\pi^0 \to \gamma\gamma$ candidates to construct $B^0 \to \pi^+\pi^-\pi^0$ candidates. During a preselection stage, we require E_B^* to lie between 4.99 and 5.59 GeV. For the charged tracks corresponding to the $\pi^\pm$ candidates, we require a maximum momentum of 10 GeV/c, a minimum of 12 hits in the drift chamber, a maximum distance-of-closest-approach (DOCA) relative to the beamspot center in the x-y plane of 1.5 cm, and a DOCA along the z axis between -10 and $+10$ cm. We require the two photon candidates that form the π^0 candidate to have an energy in the laboratory frame between 30 MeV and 10 GeV, and lateral moments in the electromagnetic calorimeter less than 0.8. We require a $\pi^0 \to \gamma\gamma$ mass between 100 and 160 MeV/c^2, and a total $\gamma\gamma$ laboratory energy greater than 200 MeV.

B. Primary selection criteria

Following preselection, we require $m_{\rm ES}$ to lie between 5.200 and 5.288 GeV/c^2. For the charged tracks corresponding to the $\pi^\pm$ candidates, we require a minimum transverse momentum of 0.1 GeV/c. The lateral moments of the two photons from the π^0 candidate are each required to lie between 0.01 and 0.60, while the laboratory-frame energies in the electromagnetic calorimeter are required to exceed 50 MeV. The mass of the π^0 candidate ($m_{\gamma\gamma}$) is required to satisfy $110 < m_{\pi^0} < 160$ MeV/c^2.

We calculate Δt by measuring the distance along the beam axis between the $B_{3\pi}$ and $B_{\rm tag}$ decay vertices and using the boost ($\beta\gamma \approx 0.56$) of the e^+e^- system. The time difference Δt and its estimated uncertainty are required to satisfy $|\Delta t| < 20$ ps and $\sigma(\Delta t) < 2.5$ ps.

The average number of B candidates (measured as the total number of candidates that pass all the preceding selection criteria divided by the total number of events with at least one candidate) is 1.45. To retain only one B-decay candidate in each event, we select the candidate that has a $\pi^0 \to \gamma\gamma$ candidate mass closest to the world average value of the π^0 mass. In the case of multiple B candidates reconstructed with the same π^0 candidate, we select one B candidate arbitrarily. A tighter requirement of $5.272 < m_{\rm ES} < 5.288$ GeV/c^2 is applied after selecting a single candidate in each event.

We use a lower $m_{\rm ES}$ sideband of on-resonance data, $5.215 < m_{\rm ES} < 5.270$ GeV/c^2, as well as off-resonance data, to model the distribution of continuum events.

C. Transformed $\Delta E'$ definition and selection criterion

Because the width of the ΔE distribution is highly correlated with the $\pi^+\pi^-$ mass and hence varies across the DP, we introduce the dimensionless transformed variable $\Delta E' = (2\Delta E - \Delta E_+ - \Delta E_-)/(\Delta E_+ - \Delta E_-)$, where $\Delta E_\pm(m_{\pi^+\pi^-}) = c_\pm - (c_\pm \mp \bar{c})(m_{\pi^+\pi^-}/m^{\rm max}_{\pi^+\pi^-})^2$, $m_{\pi^+\pi^-}$ is the measured $\pi^+\pi^-$ mass, and the parameter $m^{\rm max}_{\pi^+\pi^-}$ is fixed at 5.0 GeV/c^2 (corresponding roughly to the maximum observed value of $m_{\pi^+\pi^-}$). The $\bar{c}$ and $c_\pm$ parameters are calculated from fits to $B^0 \to \rho^+\pi^-$ signal MC. The dimensionless quantity $\Delta E'$ serves to reduce the degree of correlation with $m_{\pi^+\pi^-}$ and is included as an input variable in the final fit.

To calculate the three c parameters, signal MC events are divided into seven equal-sized bins in $m_{\pi^+\pi^-}$ from 0 to 5.143 GeV/c^2. In each mass bin, the peak in ΔE is fit with the sum of two Gaussians, and the mean (μ) and width (σ) of the narrower Gaussian are extracted. From these parameters, two sets of data points are constructed: one consisting of the values of $\mu + 3\sigma$ for each mass bin and the other consisting of the values of $\mu - 3\sigma$ for each mass bin. The first set is fit with the quadratic function corresponding to $\Delta E_+(m_{\pi^+\pi^-})$, which yields values for c_+ and $\bar{c}$. A similar fit is performed on the second set using the function $\Delta E_-(m_{\pi^+\pi^-})$, which yields values for c_- and $\bar{c}$. The $\bar{c}$ value used in the final transformation is obtained by averaging the $\bar{c}$ values from the separate fits. For the final calculation of $\Delta E'$, we use the parameter values $\bar{c} = 0.0792$ GeV, $c_- = -0.1433$ GeV, and $c_+ = 0.1093$ GeV. Candidates are selected if $\Delta E'$ is between -1 and $+1$, which is roughly a $\pm 3\sigma$ criterion on ΔE.

D. Particle identification selection criteria

In the previous *BABAR* analysis [2], the charged pion candidates were required to be inconsistent with muon, kaon, proton, and electron hypotheses. Improvements in the *BABAR* reconstruction software now provide decreased false-positive rates for a given signal efficiency. We apply a PID selection criterion corresponding to a signal-to-square-root-of-background ($S/\sqrt{B}$) ratio (calculated using off-resonance data to model background, and correctly reconstructed $B^0 \to \rho^\pm\pi^\mp$ signal MC to model signal) of 1.26 (scaled relative to all previous selection criteria). For comparison, application of the PID criteria of the previous analysis achieves a scaled $S/\sqrt{B}$ ratio of 1.14. The new PID criterion selects 54.6% of off-resonance data and 93.2% of correctly reconstructed signal MC events relative to the previous selection criteria.

E. Multivariate discriminator selection

Continuum $q\bar{q}$ events are the primary source of background in this analysis. To improve discrimination between continuum background and signal events, we train a neural network (NN) on off-resonance data and signal MC using the "MLP" (multi-layer perceptron) NN implementation in the TMVA software package [13]. The NN is trained using 10,000 events representative of signal, 7500 events representative of background, and 200 training iterations. Validation is performed using an independent sample of 20000 signal and 7500 background events. The NN is configured to use two hidden layers with six and five nodes, respectively. The NN uses four event-shape variables that help distinguish between the roughly isotropic shape of B decays and the more jetlike shape of continuum events. The training variables include the Legendre moment L0 of the rest of the event, defined as the sum of the magnitudes of the momenta of all charged particle candidates not belonging to the reconstructed B candidate; the ratio of the Legendre moment L2 to the Legendre moment L0, where L2 is defined as the sum over all tracks and neutral clusters not belonging to the B candidate of $p \cdot (3\cos^2\theta - 1)/2$ where p is the magnitude of the momentum of each track or cluster and θ is the angle between the B thrust axis and the momentum corresponding to the track or cluster; the cosine of the angle between the B candidate momentum and the beam axis; and the cosine of the angle between the thrust axis of the B candidate and the beam axis. All of these input variables are calculated in the CM frame.

While optimizing the NN discriminator, we studied whether some improvement in performance might be achieved by training the discriminator separately in each of seven B-flavor tagging categories (each of which has a different flavor tagging purity), or applying NN selection criteria separately in each of the B-flavor tagging categories. These approaches were found to yield negligible improvements in signal efficiency for a given degree of background rejection.

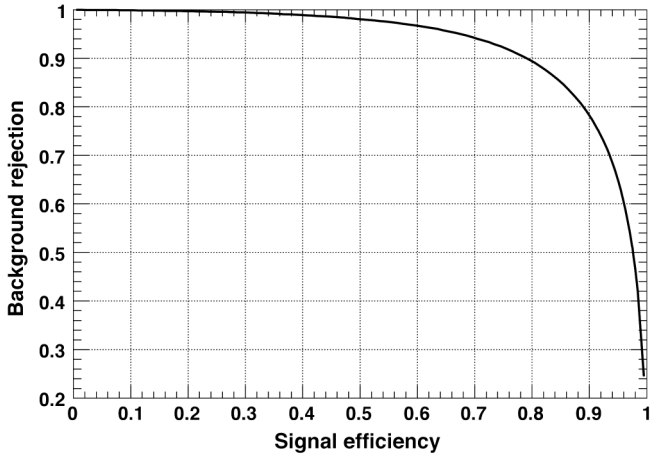

FIG. 2. $B^0 \to \rho^{\pm}\pi^{\mp}$ continuum background rejection versus signal efficiency for final neural network implementation, with continuum background represented by off-resonance data, and signal represented by signal MC. Points on the curve correspond to different requirements on the neural network output. Our selection criterion retains 75% of signal events.

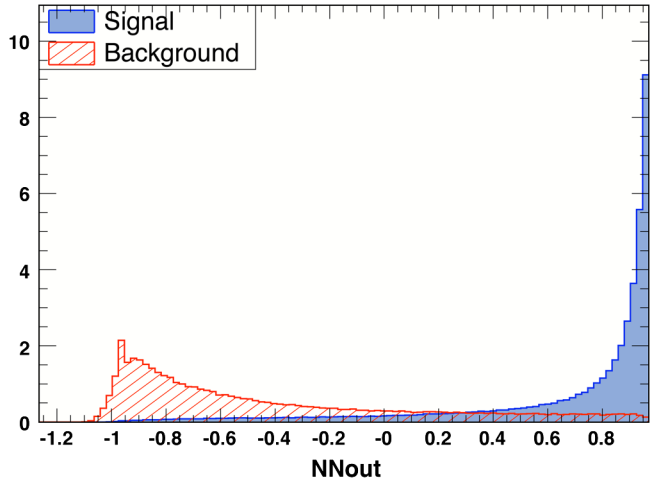

FIG. 3 (color online). NN output distributions for signal $B^0 \to \rho^{\pm}\pi^{\mp}$ (solid blue) and continuum background (hatched red) with an arbitrary vertical scale. Continuum background is represented by off-resonance data while signal is represented by signal MC. Our selection criterion requires NN > 0.58.

The final performance of the NN discriminator is shown in Fig. 2, while Fig. 3 shows the separation achieved between signal and background samples during training. The NN is used to apply a loose selection criterion that retains 75% of the signal events remaining after all previous selection criteria. The NN output is also used as an input variable in the final fit.

F. Selection performance

Table II provides a summary of the signal efficiencies for each step of the selection process for simulated

TABLE II. Selection efficiencies, $\epsilon_X^{\rm MC}$, relative to previous criteria for simulated $B^0 \to X$ events ($X = \rho^+\pi^-$, $\rho^0\pi^0$, nonresonant $\pi^+\pi^-\pi^0$). Statistical uncertainties on all efficiencies are less than 0.001.

Cuts	$\epsilon^{\rm MC}_{\rho^+\pi^-}$	$\epsilon^{\rm MC}_{\rho^0\pi^0}$	$\epsilon^{\rm MC}_{\pi^+\pi^-\pi^0}$
Preselection	0.650	0.582	0.547
$p_T > 0.1$ GeV	0.994	0.986	0.999
$\lvert\Delta t\rvert < 20$ ps & $\sigma(\Delta t) < 2.5$ ps	0.966	0.957	0.960
Photon energy and lateral mom.	0.928	0.960	0.943
$110 < m(\gamma\gamma) < 160$ MeV/c^2	0.982	0.983	0.983
PID	0.920	0.936	0.928
$5.200 < m_{\rm ES} < 5.288$ GeV/c^2	0.994	0.995	0.996
$-1 < \Delta E' < 1$	0.819	0.863	0.871
NN > 0.58	0.749	0.768	0.762
$5.272 < m_{\rm ES} < 5.288$ GeV/c^2	0.798	0.826	0.937
Cumulative efficiency	0.255	0.265	0.279

$B^0 \to \rho^+\pi^-$, $B^0 \to \rho^0\pi^0$, and nonresonant (three-body phase space) $B^0 \to \pi^+\pi^-\pi^0$ events.

VI. MAXIMUM LIKELIHOOD FIT

We perform an unbinned extended maximum likelihood fit to the selected events in order to extract the event yields and the U and I parameters. The input variables are $m_{\rm ES}$, $\Delta E'$, the NN output, and the three time-dependent-SDP variables m', θ', and Δt. We also use $\sigma_{\Delta t}$ (the per-event uncertainty on Δt) as a scale factor in the signal Δt resolution function. The likelihood function used in the fit consists of separate components for signal, continuum background, charged B backgrounds, and neutral B backgrounds. The signal PDF is subdivided into components describing correctly reconstructed or ''truth-matched'' (TM), and misreconstructed or self-cross-feed (SCF) candidates. Truth-matched events are identified using MC generator information and contain correctly reconstructed π^+, π^-, and π^0 candidates, two of which were produced in a ρ decay. It is also required that the ρ and the remaining π come from the same B-meson parent. For nonresonant MC, we instead require that all three pions come directly from the same B parent with no intermediate ρ resonance. All signal events that are not TM are SCF. In $B^0 \to \rho^\pm\pi^\mp$ MC, 22% of reconstructed B candidates are SCF while in $B^0 \to \rho^0\pi^0$ MC, 14% are SCF.

The signal and B-background components are further divided by B-flavor tagging category and the flavor of the tag-side B. The $B_{\rm tag}$ flavor is estimated using multivariate discriminator techniques and is classified as belonging to one of seven flavor-tagging categories corresponding to different degrees of probability that the flavor has been correctly determined [14].

Additionally, prior to the final fit, a transformation is applied to the NN variable. This has the effect of broadening the peak in the signal NN distribution, and transforming the continuum NN distribution to make fitting with the smoothing algorithm (see Sec. VI B) more effective. The transformation is defined by

$$\mathrm{NN}_{\rm new} = 1 - \arccos\left(\mathrm{NN}_{\rm old} + \beta\right), \tag{27}$$

where $\beta = 0.029$ is an offset approximately equal to 1 minus the maximum of the original NN distribution.

A. Likelihood function

The PDF $\mathcal{P}_i^c$ for an event i in tagging category c is the sum of the probability densities of all the signal and background components, namely,

$$\begin{aligned}\mathcal{P}_i^c \equiv\ & N_{3\pi} f_{3\pi}^c [(1 - \bar{f}_{\rm SCF}^c)\mathcal{P}_{3\pi-{\rm TM},i}^c + \bar{f}_{\rm SCF}^c \mathcal{P}_{3\pi-{\rm SCF},i}^c] \\ & + N_{q\bar{q}}^c \frac{1}{2}(1 + q_{{\rm tag},i} A_{q\bar{q},{\rm tag}})\mathcal{P}_{q\bar{q},i}^c \\ & + \sum_{j=1}^{N_{\rm class}^{B^+}} N_{B^+ j} f_{B^+ j}^c \frac{1}{2}(1 + q_{{\rm tag},i} A_{B^+,{\rm tag},j})\mathcal{P}_{B^+,ij}^c \\ & + \sum_{j=1}^{N_{\rm class}^{B^0}} N_{B^0 j} f_{B^0 j}^c \mathcal{P}_{B^0,ij}^c, \end{aligned} \tag{28}$$

where

(i) $N_{3\pi}$ is the total number of $\pi^+\pi^-\pi^0$ signal events in the data sample (both TM and SCF);
(ii) $f_{3\pi}^c$ is the fraction of signal events (TM and SCF) in flavor tagging category c;
(iii) $\bar{f}_{\rm SCF}^c$ is the fraction of misreconstructed signal events (SCF) in tagging category c;
(iv) $\mathcal{P}_{3\pi-{\rm TM},i}^c$ and $\mathcal{P}_{3\pi-{\rm SCF},i}^c$ are the products of PDFs of the discriminating variables used in tagging category c for TM and SCF events, respectively;
(v) $N_{q\bar{q}}^c$ is the number of continuum events in flavor tagging category c;
(vi) $q_{{\rm tag},i}$ is the tag flavor of the event where we use the convention that $q_{{\rm tag},i} = 1$ for $B_{\rm tag} = B^0$ and $q_{{\rm tag},i} = -1$ for a $B_{\rm tag} = \bar{B}^0$;
(vii) $A_{q\bar{q},{\rm tag}}$ is the flavor tag asymmetry, parametrizing possible charge asymmetry in continuum events;
(viii) $\mathcal{P}_{q\bar{q},i}^c$ is the continuum PDF for tagging category c;
(ix) $N_{\rm class}^{B^+}$ ($N_{\rm class}^{B^0}$) is the number of charged (neutral) B-background classes included in the fit (including generic modes); see Table I;
(x) $N_{B^+ j}$ ($N_{B^0 j}$) is the number of expected events in the charged (neutral) B-background class j;
(xi) $f_{B^+ j}^c$ ($f_{B^0 j}^c$) is the fraction of charged (neutral) B-background events of class j that are in flavor tagging category c;
(xii) $A_{B^+,{\rm tag},j}$ is the flavor tag asymmetry of charged B-background class j;
(xiii) $\mathcal{P}_{B^+,ij}^c$ is the B^+-background PDF for tagging category c and class j;
(xiv) $\mathcal{P}_{B^0,ij}^c$ is the B^0-background PDF for tagging category c and class j.

The PDFs $\mathcal{P}_X^c$ are the product of PDFs for the discriminating variables $x_1 = m_{\rm ES}$, $x_2 = \Delta E'$, $x_3 = \mathrm{NN}_{\rm new}$, and the three time-dependent-SDP variables $x_4 = \{m', \theta', \Delta t\}$,

$$\mathcal{P}_{X,i(j)}^c \equiv \prod_{k=1}^{4} \mathcal{P}_{X,i(j)}^c(x_k). \tag{29}$$

The extended likelihood function including all tagging categories is given by

$$\mathcal{L} \equiv \prod_{c=1}^{7} e^{-\bar{N}^c} \prod_{i=1}^{N^c} \mathcal{P}_i^c, \tag{30}$$

where $\bar{N}^c$ is the total number of events expected in tagging category c and N^c is the observed number.

B. Signal parametrization

The effect of experimental resolution for Δt in signal events is taken into account by convolving the PDF describing the true Δt distribution with a sum of three Gaussians.

The triple-Gaussian resolution function is constructed using a narrow "core" Gaussian, a slightly wider "tail" Gaussian, and a very wide "outlier" Gaussian. In the final fit to on-resonance data, all signal Δt parameters are fixed to values obtained from fits to fully reconstructed B decays. In the fits to fully reconstructed B decays, the mean and width of the outlier Gaussian are fixed to 0 and 8 ps, respectively. Similarly, the width of the tail Gaussian is fixed to 3 ps, but its mean is allowed to vary. Finally, both the mean and width of the core Gaussian are allowed to vary in the fit, and the means of the core Gaussian are allowed to take on different values in each B-flavor tagging category. The means and widths of the core and tail Gaussians are scaled by the per-event uncertainty on Δt ($\sigma_{\Delta t}$),

$$\begin{aligned}\mathcal{R}_{\rm sig}(\Delta t, \sigma_{\Delta t}) = {} & (1 - f_{\rm tail} - f_{\rm out}) G(\Delta t; s^b_{\rm core}\sigma_{\Delta t}, s^\sigma_{\rm core}\sigma_{\Delta t}) \\ & + f_{\rm tail} G(\Delta t, s^b_{\rm tail}\sigma_{\Delta t}; s^\sigma_{\rm tail}\sigma_{\Delta t}) \\ & + f_{\rm out} G(\Delta t; s^b_{\rm out}, \sigma_{\rm out}),\end{aligned} \tag{31}$$

where $G(x; x_0, \sigma)$ is a Gaussian with mean x_0 and width σ. See Fig. 4 (upper plot) for the distribution of Δt in signal MC events.

The $\Delta E'$ signal distribution is modeled using the sum of two Gaussians where all five free parameters depend linearly on $m^2(\pi^+\pi^-)$ in order to account for residual dependence on the mass. The $m_{\rm ES}$ signal distribution is parametrized using a bifurcated Crystal Ball function, which is composed of a one-sided Gaussian and a Crystal Ball function:

$$f(x) = \begin{cases} Ce^{-(x-m)^2/2s_R^2} & \text{for } (x-m) > 0, \\ Ce^{-(x-m)^2/2s_L^2} & \text{for } -A < \frac{x-m}{s_L} < 0, \\ C\left(\frac{b}{A}\right)^b e^{-\frac{A^2}{2}} \left(\frac{b}{A} - A - \frac{x-m}{s_L}\right)^{-b} & \text{for } \frac{x-m}{s_L} < -A. \end{cases} \tag{32}$$

The parameters describing both these line shapes are extracted from fits to signal MC events. In the final fit, the parameter m is free to vary for $m_{\rm ES}$ while the core Gaussian mean and width, and the slope of the mean [i.e., the dependence of the mean on $m^2(\pi^+\pi^-)$] are free to vary for $\Delta E'$.

The $\mathrm{NN}_{\rm new}$ signal distribution is modeled by nonparametric histograms generated by smoothing the $\mathrm{NN}_{\rm new}$ distribution in signal MC.

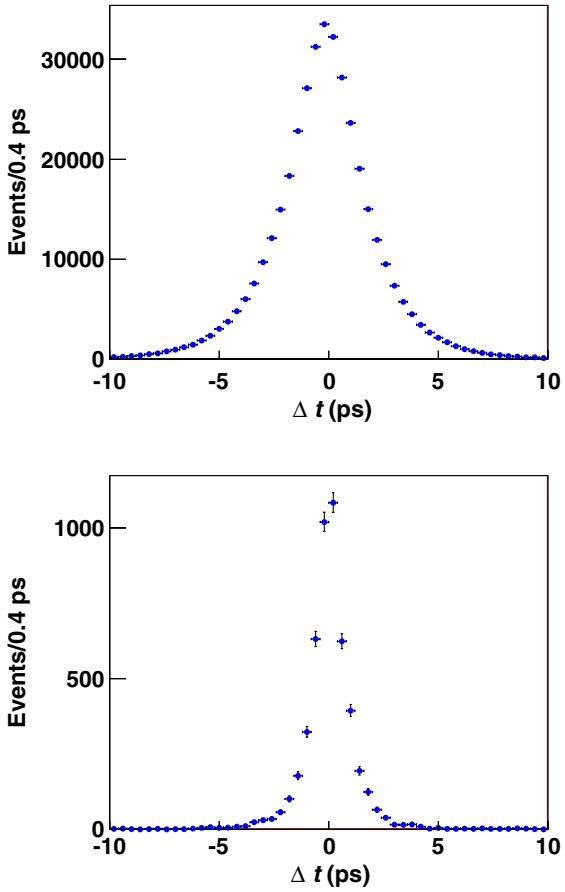

FIG. 4 (color online). Distribution of Δt in simulated $B^0 \to \rho^\pm \pi^\mp$ signal events (top) and in off-resonance data (bottom).

The $\Delta E'$ distribution for SCF signal candidates is described using a single Gaussian with mean and width fixed to the values extracted from a fit to SCF signal MC.

The distributions of $m_{\rm ES}$ and $\mathrm{NN}_{\rm new}$ for SCF signal events are modeled with nonparametric histograms generated by smoothing the appropriate one-dimensional distributions in SCF signal MC. The nonparametric PDFs for the $\mathrm{NN}_{\rm new}$ distributions in both TM and SCF signal are generated separately for each flavor-tagging category.

While the SDP distribution for TM signal events is parametrized by the full time-dependent decay probability, the SCF distribution is parametrized by modifying this distribution. Using signal MC, we create a binned map in the SDP that contains the probability for an event generated in each bin of the SDP to be reconstructed in the same bin, or each of the other bins. This map is convolved with the time-dependent decay PDF to generate the SCF signal PDF in the SDP.

C. Continuum background parametrization

The Δt distribution for continuum background is modeled using a sum of three Gaussians. The parameters of this triple Gaussian are obtained from a fit to off-resonance data in which all parameters are allowed to vary. See

Fig. 4 (lower plot) for the distribution of Δt in off-resonance data.

The $\Delta E'$ distribution for continuum background is modeled using a second-order polynomial with parameter values extracted from a fit to the $m_{\rm ES}$ sideband in on-resonance data.

The distribution of $m_{\rm ES}$ for continuum background is modeled using an Argus [15] function with shape and endpoint parameters that are allowed to vary in the final fit.

To account for residual dependence on DP position, the distribution of $\mathrm{NN}_{\rm new}$ for continuum background is modeled using a second-order polynomial function in which each coefficient depends linearly on $m_{\rm dist}$, the minimum invariant mass of any $\pi\pi$ combination in the $B^0 \to \pi^+\pi^-\pi^0$ candidate, which acts as a measure of the distance from the edge of the DP. In addition, the polynomial is multiplied by $(1 - \mathrm{NN}_{\rm new})^a$ where a is a linear function of $m_{\rm dist}$. All the polynomial parameters are free to vary in the final fit.

The two-dimensional SDP distribution for continuum events is obtained by applying Gaussian kernel smoothing algorithms to the SDP distribution for on-resonance $m_{\rm ES}$ sideband data and generating a two-dimensional histogram from the resulting PDF, which serves as a nonparametric PDF in the fit. Histogram PDFs are generated separately for each flavor-tagging category and, within each category, for both B-flavor tags. Bins in these histograms are mirrored across the $\theta' = 0.5$ axis so that the distributions are symmetric in θ'. A number of parameters are allowed to vary in the fit to allow for an asymmetry.

D. B-background parametrization

The functional form of the Δt resolution functions for the B backgrounds is the same as that for signal. Parameter values are obtained from separate fits to fully simulated MC data samples representative of each B-background class.

Simulated samples for each of the B-background classes are used to generate nonparametric PDFs for use in the final fit. One-dimensional PDFs are used for $\Delta E'$, $m_{\rm ES}$, and $\mathrm{NN}_{\rm new}$, without any splitting by flavor-tagging category. Two-dimensional SDP PDFs are generated for each B-background class and each B-flavor tag within that class.

E. Dalitz-plot-dependent selection efficiency

Selection efficiencies across the SDP are calculated from a combination of all available nonresonant ($B^0 \to \pi^+\pi^-\pi^0$), $B^0 \to \rho^\pm\pi^\mp$, and $B^0 \to \rho^0\pi^0$ MC samples. We divide the SDP into a 40 by 40 grid and, for each bin, calculate both the fraction of events generated in that bin that are correctly reconstructed (TM), and the fraction of events generated in that bin that are misreconstructed (SCF). From this, we generate tables of efficiencies that are used as inputs to the fit. Histograms of the TM and SCF selection efficiencies are provided in Fig. 5.

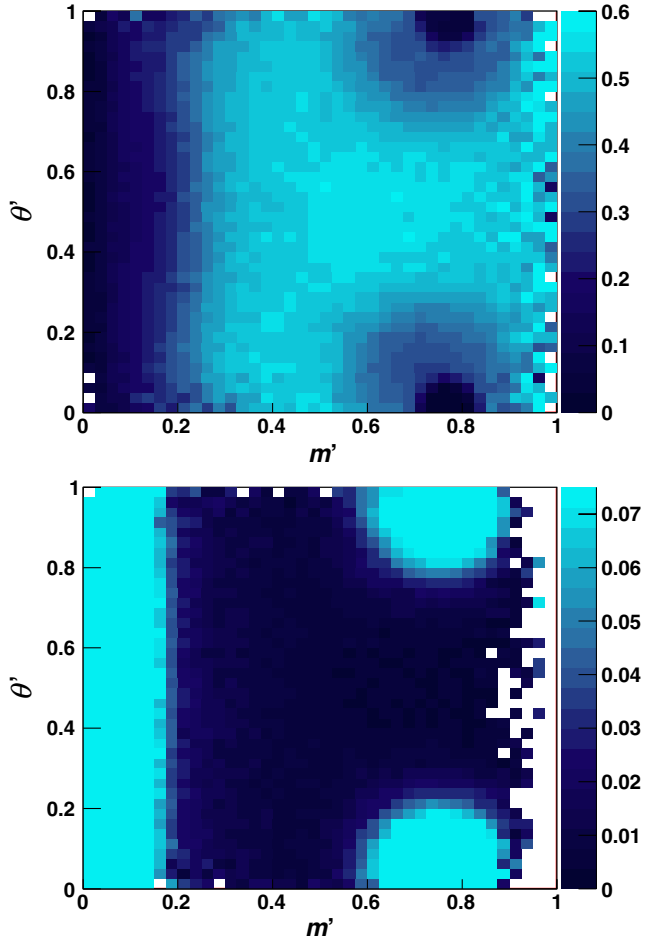

FIG. 5 (color online). Square Dalitz plot map of TM (top) and SCF (bottom) selection efficiencies. The color scale on the TM plot has a maximum of 0.60 while that on the SCF plot has a maximum of 0.075.

VII. SYSTEMATIC STUDIES

A. The effect of the $\rho(1700)$

We include the $\rho(1450)$ in the final fit with an assumption that the relative magnitudes and phases between the three $\rho(1450)$ resonances are the same as for the $\rho(770)$. Whereas there is reasonable motivation for this assumption in the case of the $\rho(1450)$ since the $\rho(770)$ and $\rho(1450)$ have the same quantum numbers, the $\rho(1700)$ does not share these quantum numbers ($\ell = 2$ instead of 0). Since the $\rho(1700)$ is not expected to provide a large contribution, we exclude the $\rho(1700)$ from the fit and associate a systematic uncertainty with this omission.

Naively, one might calculate this systematic uncertainty by fitting the full data set with and without the $\rho(1700)$ and calculating a single change in the U and I parameters, but this approach suffers from statistical uncertainties due to the fact that there is only one data set available. Nonetheless, it is still useful to calculate a covariance matrix using this approach in order to estimate the magnitude of the systematic uncertainty. As a first order assessment of the

systematic uncertainty, we calculate a covariance matrix with elements given by

$$C_{i,j} \equiv \delta_i \delta_j, \tag{33}$$

where δ_i is the difference between the value of the ith U or I parameter in fits with and without the $\rho(1700)$. When the three $\rho(1700)$ resonances are included in the fit, their magnitudes and phases are all allowed to vary independently. The square roots of the diagonal elements of the matrix (in other words, the absolute value of the change in each U or I parameter) are given in Table III along with the ratio relative to the statistical uncertainty on each parameter in the fit without the $\rho(1700)$. The ratios are generally less than 1; only 4 of the 26 ratios are greater than 1, indicating that the changes in the U and I parameters resulting from the inclusion of a $\rho(1700)$ in the Dalitz model are mostly small.

TABLE III. Magnitude of changes in U and I parameters between fits with and without the $\rho(1700)$, the ratio of these magnitudes relative to statistical uncertainties from the fit without the $\rho(1700)$, the bootstrapped estimate of the uncertainty on changes in U and I parameters between fits with and without the $\rho(1700)$, and the ratio of the mean change in the U and I parameters across all bootstrapped fits to their bootstrap-estimated uncertainties.

Parameter	$\lvert\Delta U\rvert$	$\lvert\Delta U\rvert/\sigma_{\text{stat}}$	$\sigma^{\text{bs}}_{\Delta U}$	$\langle\Delta U\rangle/\sigma^{\text{bs}}_{\Delta U}$
I_0	0.017	0.46	0.020	−0.36
I_-	0.015	0.24	0.022	0.41
I^{Im}_{-0}	0.40	0.92	0.42	−0.70
I^{Re}_{-0}	0.39	0.67	0.7	0.28
I_+	0.0013	0.02	0.023	0.18
I^{Im}_{+0}	0.024	0.07	0.42	−0.11
I^{Re}_{+0}	0.18	0.40	0.7	0.26
I^{Im}_{+-}	1.34	1.81	0.9	−0.95
I^{Re}_{+-}	0.68	0.90	0.9	−0.59
U^-_0	0.012	0.23	0.029	0.29
U^+_0	0.006	0.21	0.017	0.54
$U^{-,\text{Im}}_{-0}$	0.31	0.70	0.5	0.76
$U^{-,\text{Re}}_{-0}$	0.31	0.89	0.34	0.49
$U^{+,\text{Im}}_{-0}$	0.14	0.70	0.21	−0.76
$U^{+,\text{Re}}_{-0}$	0.25	1.47	0.17	−0.77
U^-_-	0.00041	0.00	0.034	0.19
U^+_-	0.015	0.21	0.05	0.15
$U^{-,\text{Im}}_{+0}$	0.18	0.61	0.44	−0.10
$U^{-,\text{Re}}_{+0}$	0.20	0.62	0.36	0.50
$U^{+,\text{Im}}_{+0}$	0.039	0.24	0.16	0.51
$U^{+,\text{Re}}_{+0}$	0.005	0.03	0.17	0.05
$U^{-,\text{Im}}_{+-}$	0.6	1.23	0.8	−0.27
$U^{-,\text{Re}}_{+-}$	0.5	1.10	0.7	0.15
$U^{+,\text{Im}}_{+-}$	0.038	0.15	0.25	−0.22
$U^{+,\text{Re}}_{+-}$	0.21	0.84	0.28	−0.21
U^-_+	0.021	0.23	0.06	−0.46

To assess the uncertainties on the changes in the U and I parameters, we employ the bootstrap technique introduced by Efron [16]. This approach allows us to calculate a covariance matrix associated with the uncertainty on the

TABLE IV. Square root of the diagonal elements of the covariance matrix associated with the uncertainties on the U and I parameters due to uncertainties on B-background branching fractions. The rightmost column contains the ratio of these systematic uncertainties to the statistical uncertainties on the U and I parameters as obtained in the nominal fit.

Parameter	σ_{syst}	$\sigma_{\text{syst}}/\sigma_{\text{stat}}$
I_0	0.0035	0.09
I_-	0.007	0.11
I^{Im}_{-0}	0.012	0.03
I^{Re}_{-0}	0.017	0.03
I_+	0.0022	0.04
I^{Im}_{+0}	0.025	0.07
I^{Re}_{+0}	0.031	0.07
I^{Im}_{+-}	0.034	0.05
I^{Re}_{+-}	0.032	0.04
U^-_0	0.0011	0.02
U^+_0	0.007	0.25
$U^{-,\text{Im}}_{-0}$	0.14	0.33
$U^{-,\text{Re}}_{-0}$	0.043	0.12
$U^{+,\text{Im}}_{-0}$	0.07	0.35
$U^{+,\text{Re}}_{-0}$	0.031	0.18
U^-_-	0.009	0.09
U^+_-	0.0018	0.03
$U^{-,\text{Im}}_{+0}$	0.017	0.06
$U^{-,\text{Re}}_{+0}$	0.011	0.04
$U^{+,\text{Im}}_{+0}$	0.016	0.10
$U^{+,\text{Re}}_{+0}$	0.011	0.07
$U^{-,\text{Im}}_{+-}$	0.10	0.20
$U^{-,\text{Re}}_{+-}$	0.019	0.04
$U^{+,\text{Im}}_{+-}$	0.05	0.20
$U^{+,\text{Re}}_{+-}$	0.06	0.22
U^-_+	0.012	0.13

TABLE V. ρ line shape parameters and uncertainties used in the fits and in evaluating the uncertainties on the U and I parameters [16].

Parameter	Value [16] (MeV/c^2)
$m_{\rho(770)^\pm}$	775.5 ± 0.6
$m_{\rho(770)^0}$	773.1 ± 0.5
$\Gamma_{\rho(770)^\pm}$	148.2 ± 0.8
$\Gamma_{\rho(770)^0}$	148.0 ± 0.9
$m_{\rho(1450)}$	1409 ± 12
$\Gamma_{\rho(1450)}$	500 ± 37

U and I parameters extracted from the fits to the full data set by fitting a large number of data sets generated by sampling events with replacement from the full data set. Each of the approximately 1000 resampled data sets generated in this manner has the same number of events as the original data set and is fit with and without the $\rho(1700)$ component. For each pair of fits, the change in the U and I parameters is calculated and a covariance matrix is generated by determining the covariances of the changes in the U and I parameters in all these pairs of fits. As demonstrated by Efron, the covariance matrix obtained in this manner is an estimate of the covariance matrix associated with the uncertainty on the changes in the U and I parameters. Therefore, the square roots of the diagonal elements of this matrix are estimates of the uncertainty on the change in each U and I parameter. These uncertainties, as well as the ratio of the mean change of each U and I across all the bootstrapped fits to its estimated uncertainty (from the bootstrap), are given in the last column in Table III. As the ratios in this table demonstrate, the mean changes in the

TABLE VI. Correlations between ρ line shape parameters used in evaluating the uncertainties on the U and I parameters [16].

	$m_{\rho(770)^{\pm}}$	$m_{\rho(770)^0}$	$\Gamma_{\rho(770)^{\pm}}$	$\Gamma_{\rho(770)^0}$	$m_{\rho(1450)}$	$\Gamma_{\rho(1450)}$
$m_{\rho(770)^{\pm}}$	1.000	0.109	0.315	−0.035	0.017	−0.150
$m_{\rho(770)^0}$	0.109	1.000	0.049	0.290	0.142	−0.065
$\Gamma_{\rho(770)^{\pm}}$	0.315	0.049	1.000	0.361	0.133	0.024
$\Gamma_{\rho(770)^0}$	−0.035	0.290	0.361	1.000	0.180	0.083
$m_{\rho(1450)}$	0.017	0.142	0.133	0.180	1.000	0.779
$\Gamma_{\rho(1450)}$	−0.150	−0.065	0.024	0.083	0.779	1.000

TABLE VII. Square root of the diagonal elements of the covariance matrix associated with the uncertainties on the U and I parameters due to uncertainties on the ρ line shape. The rightmost column contains the ratio of these systematic uncertainties to the statistical uncertainties on the U and I parameters as obtained in the nominal fit.

Parameter	σ_{syst}	$\sigma_{\text{syst}}/\sigma_{\text{stat}}$
I_0	0.0005	0.01
I_-	0.0013	0.02
I_{-0}^{Im}	0.009	0.02
I_{-0}^{Re}	0.025	0.04
I_+	0.0007	0.01
I_{+0}^{Im}	0.012	0.03
I_{+0}^{Re}	0.06	0.13
I_{+-}^{Im}	0.05	0.07
I_{+-}^{Re}	0.07	0.09
U_0^-	0.0014	0.03
U_0^+	0.0020	0.07
$U_{-0}^{-,\text{Im}}$	0.029	0.07
$U_{-0}^{-,\text{Re}}$	0.018	0.05
$U_{-0}^{+,\text{Im}}$	0.020	0.10
$U_{-0}^{+,\text{Re}}$	0.017	0.10
U_-^-	0.0014	0.01
U_-^+	0.0017	0.02
$U_{+0}^{-,\text{Im}}$	0.019	0.07
$U_{+0}^{-,\text{Re}}$	0.011	0.03
$U_{+0}^{+,\text{Im}}$	0.007	0.04
$U_{+0}^{+,\text{Re}}$	0.005	0.03
$U_{+-}^{-,\text{Im}}$	0.028	0.06
$U_{+-}^{-,\text{Re}}$	0.023	0.05
$U_{+-}^{+,\text{Im}}$	0.020	0.08
$U_{+-}^{+,\text{Re}}$	0.026	0.10
U_+^-	0.0013	0.02

TABLE VIII. Magnitude of changes in U and I parameters between fits with and without the uniform background component, the ratio of these magnitudes relative to statistical uncertainties from the fit without the uniform component, the bootstrapped estimate of the uncertainty on changes in U and I parameters between fits with and without the uniform component, and the ratio of the mean change in the U and I parameters across all bootstrapped fits to their bootstrap-estimated uncertainties.

Parameter	$\lvert\Delta U\rvert$	$\lvert\Delta U\rvert/\sigma_{\text{stat}}$	$\sigma_{\Delta U}^{\text{bs}}$	$\langle\Delta U\rangle/\sigma_{\Delta U}^{\text{bs}}$
I_0	0.005	0.13	0.006	−0.62
I_-	0.006	0.10	0.007	0.55
I_{-0}^{Im}	0.041	0.10	0.16	−0.18
I_{-0}^{Re}	0.09	0.16	0.25	0.34
I_+	0.0013	0.02	0.006	0.22
I_{+0}^{Im}	0.016	0.05	0.08	−0.11
I_{+0}^{Re}	0.029	0.06	0.11	−0.07
I_{+-}^{Im}	0.006	0.01	0.17	−0.04
I_{+-}^{Re}	0.07	0.09	0.21	−0.15
U_0^-	0.000005	0.00	0.008	−0.07
U_0^+	0.0036	0.12	0.0036	0.79
$U_{-0}^{-,\text{Im}}$	0.14	0.33	0.18	−0.58
$U_{-0}^{-,\text{Re}}$	0.019	0.05	0.13	−0.03
$U_{-0}^{+,\text{Im}}$	0.06	0.31	0.06	0.64
$U_{-0}^{+,\text{Re}}$	0.026	0.16	0.06	−0.33
U_-^-	0.006	0.06	0.012	0.39
U_-^+	0.005	0.07	0.010	0.30
$U_{+0}^{-,\text{Im}}$	0.0032	0.01	0.10	0.16
$U_{+0}^{-,\text{Re}}$	0.031	0.10	0.11	0.27
$U_{+0}^{+,\text{Im}}$	0.0026	0.02	0.041	−0.08
$U_{+0}^{+,\text{Re}}$	0.006	0.04	0.044	−0.14
$U_{+-}^{-,\text{Im}}$	0.045	0.09	0.16	−0.38
$U_{+-}^{-,\text{Re}}$	0.0032	0.01	0.18	−0.05
$U_{+-}^{+,\text{Im}}$	0.043	0.16	0.06	−0.34
$U_{+-}^{+,\text{Re}}$	0.05	0.21	0.13	−0.23
U_+^-	0.007	0.07	0.012	−0.47

U and I parameters are consistent with 0. Given these results, we use the covariance matrix obtained by bootstrapping to characterize the systematic uncertainty associated with excluding the $\rho(1700)$.

B. *B* background branching fractions

We account for uncertainties on the branching fractions for the various B background classes by performing fits to data after increasing and decreasing the expected number of B background events by 10%. The value of 10% is an estimate of the degree of uncertainty on the expected number of events in the B background classes with the largest contributions (see Table I). We calculate a systematic covariance matrix for the U and I parameters from these fits. Element (i, j) is given by

$$C_{ij} \equiv \frac{\delta_i}{2}\frac{\delta_j}{2}, \tag{34}$$

where δ_i is the difference between the value of the ith U or I parameter in the fit with increased B background contributions, and the fit with decreased contributions. The systematic errors ($\sigma^i_{\rm syst} = \sqrt{C_{ii}}$) associated with the B-background branching fractions are given in Table IV. The first column of numbers contains the systematic errors calculated from the square root of the diagonal elements of the covariance matrix while the second column of numbers contains the ratio of these uncertainties to the statistical uncertainties from the nominal fit to the full data set.

TABLE IX. Systematic uncertainties for the three sources of systematic uncertainty not revisited for the present analysis. These values are taken from the 2007 *BABAR* analysis and used without modification [2].

Parameter	B Bkgnd CP	Tag Side Interference	"Others"
I_0	0.004	0.000	0.002
I_-	0.013	0.003	0.007
$I^{\rm Im}_{-0}$	0.064	0.018	0.077
$I^{\rm Re}_{-0}$	0.083	0.006	0.059
I_+	0.009	0.011	0.005
$I^{\rm Im}_{+0}$	0.050	0.003	0.065
$I^{\rm Re}_{+0}$	0.121	0.019	0.092
$I^{\rm Im}_{+-}$	0.168	0.033	0.133
$I^{\rm Re}_{+-}$	0.088	0.026	0.078
U^-_0	0.015	0.000	0.004
U^+_0	0.005	0.001	0.004
$U^{-,\rm Im}_{-0}$	0.052	0.007	0.016
$U^{-,\rm Re}_{-0}$	0.044	0.022	0.046
$U^{+,\rm Im}_{-0}$	0.038	0.022	0.011
$U^{+,\rm Re}_{-0}$	0.015	0.012	0.007
U^-_-	0.041	0.004	0.015
U^+_-	0.014	0.003	0.010
$U^{-,\rm Im}_{+0}$	0.073	0.028	0.038
$U^{-,\rm Re}_{+0}$	0.052	0.004	0.037
$U^{+,\rm Im}_{+0}$	0.042	0.001	0.032
$U^{+,\rm Re}_{+0}$	0.059	0.031	0.060
$U^{-,\rm Im}_{+-}$	0.055	0.031	0.045
$U^{-,\rm Re}_{+-}$	0.238	0.044	0.112
$U^{+,\rm Im}_{+-}$	0.028	0.031	0.012
$U^{+,\rm Re}_{+-}$	0.038	0.028	0.079
U^-_+	0.036	0.007	0.009

C. ρ line shapes

The systematic uncertainties associated with the $\rho(770)^{\pm}$, $\rho(770)^0$, and $\rho(1450)$ line shapes are calculated by varying their masses and widths according to the

TABLE X. The square root of the diagonal elements of the final systematic covariance matrix for the U and I parameters, the ratio of these total systematic errors to the statistical errors from the final fit, and the ratio of the total error (including statistical and systematic contributions) to the statistical error.

Parameter	$\sigma_{\rm syst}$	$\sigma_{\rm syst}/\sigma_{\rm stat}$	$\sqrt{\sigma^2_{\rm stat}+\sigma^2_{\rm syst}}/\sigma_{\rm stat}$
I_0	0.022	0.59	1.16
I_-	0.028	0.45	1.10
$I^{\rm Im}_{-0}$	0.5	1.08	1.47
$I^{\rm Re}_{-0}$	0.8	1.34	1.67
I_+	0.029	0.46	1.10
$I^{\rm Im}_{+0}$	0.43	1.21	1.57
$I^{\rm Re}_{+0}$	0.7	1.57	1.86
$I^{\rm Im}_{+-}$	0.9	1.26	1.61
$I^{\rm Re}_{+-}$	1.0	1.30	1.64
U^-_0	0.034	0.65	1.19
U^+_0	0.020	0.68	1.21
$U^{-,\rm Im}_{-0}$	0.5	1.19	1.56
$U^{-,\rm Re}_{-0}$	0.37	1.05	1.45
$U^{+,\rm Im}_{-0}$	0.24	1.16	1.53
$U^{+,\rm Re}_{-0}$	0.18	1.10	1.49
U^-_-	0.06	0.59	1.16
U^+_-	0.05	0.72	1.23
$U^{-,\rm Im}_{+0}$	0.5	1.59	1.88
$U^{-,\rm Re}_{+0}$	0.38	1.19	1.55
$U^{+,\rm Im}_{+0}$	0.17	1.09	1.48
$U^{+,\rm Re}_{+0}$	0.19	1.26	1.61
$U^{-,\rm Im}_{+-}$	0.8	1.68	1.95
$U^{-,\rm Re}_{+-}$	0.8	1.70	1.98
$U^{+,\rm Im}_{+-}$	0.26	1.02	1.43
$U^{+,\rm Re}_{+-}$	0.33	1.29	1.63
U^-_+	0.07	0.77	1.26

uncertainties listed in Table V and the correlation matrix in Table VI. These correlations and uncertainties were determined using a Gounaris-Sakurai model fit to data from $\tau^+ \to \bar{\nu}_\tau \rho^+ (\to \pi^+ \pi^0)$ decays and $e^+e^- \to \rho^0 \to \pi^+\pi^-$ annihilation [17]. We use updated line shape fits including new data from e^+e^- annihilation [18] and τ spectral functions [19].

The correlations between the three ρ masses and widths as well as their uncertainties were used to calculate the corresponding covariance matrix. A six-dimensional correlated Gaussian was defined with means corresponding to the central values of the line shape parameters. A set of 50 vectors of line shape parameters was sampled randomly from the multi-dimensional Gaussian distribution and used to perform 50 fits. Using the randomly sampled masses and widths, and initializing all other parameter values to those from the best fit to the full on-resonance data set with nominal parameters, we performed a fit with each resonance configuration, producing 50 final sets of U and I parameters. The covariances of these 50 sets of U and I parameter values were calculated using the set of final fit values from the nominal fit as expected values.

As a test of the fitting framework, the mean of the number of signal events from the 50 fits was extracted and compared to the nominal value. They were found to be in agreement with a difference of $0.6\sigma_{\rm stat}$ (where $\sigma_{\rm stat}$ is the statistical error on the number of signal events from the nominal fit to the full on-resonance data set), exhibiting negligible bias. As a further comparison, the ratios of the systematic errors (taken from the square root of the diagonal of the covariance matrix) to the statistical errors (taken from the nominal fit) were calculated and found to be small as shown in Table VII.

D. Uniform background contributions

The systematic uncertainties associated with incoherent uniform background contributions in the DP are calculated in the same manner as for the $\rho(1700)$. The nominal

TABLE XI. Systematic correlation matrix for the U and I parameters, including contributions from three sources of minor systematic uncertainties evaluated in the 2007 *BABAR* analysis. Elements above the diagonal are redundant and not included in the table. (Continued in Tables XII and XIII.)

	I_0	I_-	$I^{\rm Im}_{-0}$	$I^{\rm Re}_{-0}$	I_+	$I^{\rm Im}_{+0}$	$I^{\rm Re}_{+0}$	$I^{\rm Im}_{+-}$
I_0	1.00							
I_-	−0.17	1.00						
$I^{\rm Im}_{-0}$	0.13	−0.13	1.00					
$I^{\rm Re}_{-0}$	−0.07	−0.00	−0.03	1.00				
I_+	−0.20	−0.13	−0.11	−0.01	1.00			
$I^{\rm Im}_{+0}$	0.04	−0.09	0.06	0.02	0.00	1.00		
$I^{\rm Re}_{+0}$	0.21	−0.05	0.04	0.08	−0.14	0.16	1.00	
$I^{\rm Im}_{+-}$	0.13	−0.00	0.09	0.09	−0.08	0.15	0.26	1.00
$I^{\rm Re}_{+-}$	0.06	0.08	0.20	0.01	−0.31	−0.07	0.16	0.20
U^-_0	0.09	0.04	−0.13	0.08	0.10	−0.04	−0.09	−0.08
U^+_0	−0.11	0.10	−0.07	0.08	0.09	−0.08	−0.05	−0.12
$U^{-,\rm Im}_{-0}$	0.08	−0.21	0.10	−0.31	0.01	0.05	0.01	−0.11
$U^{-,\rm Re}_{-0}$	−0.03	−0.01	−0.41	0.13	0.09	−0.01	0.03	−0.16
$U^{+,\rm Im}_{-0}$	−0.18	0.21	−0.04	0.18	0.02	−0.17	−0.11	−0.00
$U^{+,\rm Re}_{-0}$	0.19	−0.15	0.32	−0.29	−0.09	0.00	−0.03	0.15
U^-_-	−0.12	0.04	−0.08	0.15	0.05	−0.02	0.11	−0.05
U^+_-	0.01	−0.08	−0.23	0.06	0.24	0.27	0.09	−0.06
$U^{-,\rm Im}_{+0}$	−0.00	0.07	−0.11	0.21	0.01	0.04	0.45	0.14
$U^{-,\rm Re}_{+0}$	−0.07	0.11	−0.12	0.12	−0.09	−0.17	0.13	−0.11
$U^{+,\rm Im}_{+0}$	0.02	0.04	−0.08	0.11	−0.02	0.01	0.18	0.09
$U^{+,\rm Re}_{+0}$	0.06	−0.01	0.08	−0.02	−0.07	0.11	−0.07	0.08
$U^{-,\rm Im}_{+-}$	0.04	−0.01	0.19	0.04	−0.13	−0.28	0.02	0.19
$U^{-,\rm Re}_{+-}$	−0.10	0.07	0.11	−0.04	−0.15	−0.25	−0.37	−0.30
$U^{+,\rm Im}_{+-}$	0.05	−0.08	0.11	−0.20	−0.07	0.08	−0.22	0.05
$U^{+,\rm Re}_{+-}$	0.24	−0.11	0.33	−0.26	−0.17	0.15	0.07	0.16
U^-_+	0.09	−0.04	0.19	−0.07	−0.23	−0.15	−0.25	0.03

fit with the uniform background component allocates only 69.4 events to the uniform component while the number of signal events decreases by 28.8 events or 0.3σ. The changes in the U and I parameters across the fits to bootstrapped samples are not significant relative to the bootstrap-estimated uncertainties (see last column of Table VIII). Also, as in the case of the $\rho(1700)$ systematic, the changes in the U and I parameters with and without the extra component are not significant relative to the statistical uncertainties on the U and I parameters (see middle column in Table VIII).

E. Other contributions

In the 2007 *BABAR* analysis [2], the following uncertainties were considered and found to provide only small contributions to the systematic uncertainty:

(i) Uncertainties in Δm_d, the B^0 lifetime, each Δt resolution parameter, tagging fractions, self-cross-feed fractions, B-background tagging fractions, and other minor systematics.

(ii) Uncertainties on CP violation in the B backgrounds (calculated by varying the parameters describing CP violation in each B background class according to their uncertainties).

(iii) Uncertainties caused by interference between $b \to c\bar{u}d$ and $b \to \bar{u}c\bar{d}$ on the tag side.

These uncertainties are not expected to provide significantly different contributions in the current analysis. Therefore, these studies were not repeated, though their contributions to the systematic covariance matrix are included. The systematic uncertainties for these contributions, as calculated in the 2007 *BABAR* analysis, are given in Table IX.

F. Total systematic uncertainties

The square root of the diagonal elements of the total systematic covariance matrix for the U and I parameters are provided in Table X. These values include all systematic uncertainties described above, including the three sources of systematic uncertainty that were not recalculated in the present analysis. Table X also contains the ratio of the total systematic error to the statistical error from the final fit and the ratio of the total error (calculated by adding the systematic and statistical errors in quadrature) to the statistical error.

Tables XI, XII, and XIII contain the complete systematic correlation matrix for the U and I parameters. Because the three additional sources of systematic uncertainty taken from our previous analysis have small contributions, and only the diagonal elements of their covariance matrix are available to us, we only use the diagonal elements when creating the total systematic covariance

TABLE XII. (Continued from Table XI) Systematic correlation matrix for the U and I parameters, including contributions from three sources of minor systematic uncertainties evaluated in the 2007 *BABAR* analysis. Elements above the diagonal are redundant and not included in the table. (Continued in Table XIII.)

	I^{Re}_{+-}	U^{-}_{0}	U^{+}_{0}	$U^{-,\mathrm{Im}}_{-0}$	$U^{-,\mathrm{Re}}_{-0}$	$U^{+,\mathrm{Im}}_{-0}$	$U^{+,\mathrm{Re}}_{-0}$	U^{-}_{-}	U^{+}_{-}
I^{Re}_{+-}	1.00								
U^{-}_{0}	−0.22	1.00							
U^{+}_{0}	0.07	0.07	1.00						
$U^{-,\mathrm{Im}}_{-0}$	0.05	−0.14	−0.17	1.00					
$U^{-,\mathrm{Re}}_{-0}$	−0.18	0.11	−0.04	−0.09	1.00				
$U^{+,\mathrm{Im}}_{-0}$	0.02	0.08	0.35	−0.49	0.04	1.00			
$U^{+,\mathrm{Re}}_{-0}$	0.36	−0.15	−0.03	0.26	−0.34	−0.14	1.00		
U^{-}_{-}	0.01	−0.07	0.04	−0.05	0.07	0.05	−0.22	1.00	
U^{+}_{-}	−0.58	0.24	0.01	−0.13	0.24	−0.04	−0.40	0.05	1.00
$U^{-,\mathrm{Im}}_{+0}$	0.05	−0.14	0.02	−0.12	0.09	0.03	−0.20	0.18	0.12
$U^{-,\mathrm{Re}}_{+0}$	−0.07	−0.04	0.03	−0.12	0.12	0.10	−0.27	0.16	0.04
$U^{+,\mathrm{Im}}_{+0}$	−0.02	0.11	−0.18	−0.12	0.16	−0.00	−0.07	0.02	−0.00
$U^{+,\mathrm{Re}}_{+0}$	−0.07	−0.12	−0.26	0.06	−0.12	−0.21	−0.01	−0.02	−0.02
$U^{-,\mathrm{Im}}_{+-}$	0.45	−0.14	0.06	0.08	−0.18	0.08	0.35	−0.13	−0.57
$U^{-,\mathrm{Re}}_{+-}$	0.27	−0.06	0.16	0.08	−0.11	0.12	0.17	−0.06	−0.48
$U^{+,\mathrm{Im}}_{+-}$	0.02	0.02	−0.26	0.21	−0.16	−0.27	0.23	−0.20	−0.17
$U^{+,\mathrm{Re}}_{+-}$	0.33	−0.15	−0.13	0.34	−0.34	−0.29	0.48	−0.19	−0.29
U^{-}_{+}	0.28	−0.14	−0.06	0.20	−0.20	−0.02	0.30	−0.23	−0.42

TABLE XIII. (Continued from Table XII) Systematic correlation matrix for the U and I parameters, including contributions from three sources of minor systematic uncertainties evaluated in the 2007 *BABAR* analysis. Elements above the diagonal are redundant and not included in the table.

	$U_{+0}^{-,\mathrm{Im}}$	$U_{+0}^{-,\mathrm{Re}}$	$U_{+0}^{+,\mathrm{Im}}$	$U_{+0}^{+,\mathrm{Re}}$	$U_{+-}^{-,\mathrm{Im}}$	$U_{+-}^{-,\mathrm{Re}}$	$U_{+-}^{+,\mathrm{Im}}$	$U_{+-}^{+,\mathrm{Re}}$	U_{+}^{-}
$U_{+0}^{-,\mathrm{Im}}$	1.00								
$U_{+0}^{-,\mathrm{Re}}$	0.15	1.00							
$U_{+0}^{+,\mathrm{Im}}$	0.06	−0.01	1.00						
$U_{+0}^{+,\mathrm{Re}}$	−0.04	−0.03	−0.10	1.00					
$U_{+-}^{-,\mathrm{Im}}$	−0.08	−0.08	0.07	−0.04	1.00				
$U_{+-}^{-,\mathrm{Re}}$	−0.25	0.05	−0.05	−0.07	0.18	1.00			
$U_{+-}^{+,\mathrm{Im}}$	−0.29	−0.19	−0.01	0.05	0.02	0.15	1.00		
$U_{+-}^{+,\mathrm{Re}}$	−0.16	−0.21	−0.13	0.14	0.16	0.09	0.28	1.00	
U_{+}^{-}	−0.19	−0.16	−0.05	0.01	0.42	0.28	0.24	0.28	1.00

matrix that is used, in turn, to generate the total correlation matrix.

VIII. RESULTS

The final values of the U and I parameters extracted from the extended maximum likelihood fit to the full on-resonance data set are provided in Table XIV. Tables XV, XVI, and XVII present the statistical correlation matrix for the U and I parameters in the fit. From an on-resonance data set containing 53084 events, the fit extracts 2940 ± 100 signal events and 46750 ± 220 continuum events. The goodness of fit is illustrated in Fig. 6, which shows overlaid distributions of fit variables in the data used in the final fit and in a parametrized MC sample generated using the results of the final fit and equivalent to 10 times the integrated luminosity of the data sample. The signal component of these plots is enhanced by a restrictive selection criterion on the NN variable. A study of the U and I parameters (see Appendix A 1) establishes that there is negligible bias in their extraction and good robustness in the presence of statistical fluctuations.

A. Quasi-two-body parameters

The U and I parameters and associated correlations can be used to extract the values of the Q2B $B^0(\bar{B}^0) \to \rho^{\pm}\pi^{\mp}$ CP-violation parameters in the time-dependent decay rate defined in Ref. [7],

$$f_{Q_{\mathrm{tag}}}^{\rho^{\pm}\pi^{\mp}}(\Delta t) = (1 \pm \mathcal{A}_{\rho\pi})\frac{e^{-|\Delta t|/\tau}}{4\tau}[1 + Q_{\mathrm{tag}}(\mathcal{S} \pm \Delta\mathcal{S}) \times \sin(\Delta m_d \Delta t) - Q_{\mathrm{tag}}(\mathcal{C} \pm \Delta\mathcal{C}) \times \cos(\Delta m_d \Delta t)], \quad (35)$$

where $Q_{\mathrm{tag}} = +1(-1)$ when the tag-side B meson is a B^0 ($\bar{B}^0$). The time- and flavor-integrated charge asymmetry $\mathcal{A}_{\rho\pi}$ quantifies direct CP violation, while $\mathcal{S}$ and $\mathcal{C}$ parametrize mixing-induced CP violation related to the angle α, and flavor-dependent direct CP violation, respectively. The parameter $\Delta\mathcal{C}$ describes the asymmetry between the rates $\Gamma(B^0 \to \rho^+\pi^-) + \Gamma(\bar{B}^0 \to \rho^-\pi^+)$ and $\Gamma(B^0 \to \rho^-\pi^+) + \Gamma(\bar{B}^0 \to \rho^+\pi^-)$, while $\Delta\mathcal{S}$ relates to the strong-phase difference between the different amplitudes involved

TABLE XIV. U and I parameter values from the final fit to the complete on-resonance data set, where the first error is statistical and the second is systematic.

Parameter	Final Fit Value
I_0	$-0.042 \pm 0.038 \pm 0.022$
I_-	$-0.00 \pm 0.06 \pm 0.03$
I_{-0}^{Im}	$-0.61 \pm 0.43 \pm 0.46$
I_{-0}^{Re}	$0.4 \pm 0.6 \pm 0.8$
I_+	$0.05 \pm 0.06 \pm 0.03$
I_{+0}^{Im}	$-0.04 \pm 0.36 \pm 0.43$
I_{+0}^{Re}	$0.5 \pm 0.5 \pm 0.7$
I_{+-}^{Im}	$-0.5 \pm 0.7 \pm 0.9$
I_{+-}^{Re}	$-0.6 \pm 0.8 \pm 1.0$
U_0^-	$0.04 \pm 0.05 \pm 0.03$
U_0^+	$0.225 \pm 0.030 \pm 0.020$
$U_{-0}^{-,\mathrm{Im}}$	$0.53 \pm 0.44 \pm 0.52$
$U_{-0}^{-,\mathrm{Re}}$	$0.49 \pm 0.35 \pm 0.37$
$U_{-0}^{+,\mathrm{Im}}$	$-0.39 \pm 0.20 \pm 0.24$
$U_{-0}^{+,\mathrm{Re}}$	$-0.05 \pm 0.17 \pm 0.18$
U_-^-	$-0.27 \pm 0.10 \pm 0.06$
U_-^+	$1.22 \pm 0.07 \pm 0.05$
$U_{+0}^{-,\mathrm{Im}}$	$0.10 \pm 0.29 \pm 0.45$
$U_{+0}^{-,\mathrm{Re}}$	$0.30 \pm 0.32 \pm 0.38$
$U_{+0}^{+,\mathrm{Im}}$	$0.41 \pm 0.16 \pm 0.17$
$U_{+0}^{+,\mathrm{Re}}$	$0.01 \pm 0.15 \pm 0.19$
$U_{+-}^{-,\mathrm{Im}}$	$1.1 \pm 0.5 \pm 0.8$
$U_{+-}^{-,\mathrm{Re}}$	$-0.5 \pm 0.5 \pm 0.8$
$U_{+-}^{+,\mathrm{Im}}$	$-0.07 \pm 0.26 \pm 0.26$
$U_{+-}^{+,\mathrm{Re}}$	$-0.19 \pm 0.25 \pm 0.33$
U_+^-	$0.25 \pm 0.09 \pm 0.07$

TABLE XV. Statistical correlation matrix for the U and I parameters. Elements above the diagonal are redundant and not included in the table. (Continued in Tables XVI and XVII.)

	I_0	I_-	I^{Im}_{-0}	I^{Re}_{-0}	I_+	I^{Im}_{+0}	I^{Re}_{+0}	I^{Im}_{+-}
I_0	1.00							
I_-	−0.04	1.00						
I^{Im}_{-0}	0.00	−0.06	1.00					
I^{Re}_{-0}	−0.05	0.05	0.05	1.00				
I_+	−0.02	−0.01	0.00	−0.00	1.00			
I^{Im}_{+0}	−0.03	−0.01	0.01	−0.01	0.05	1.00		
I^{Re}_{+0}	−0.12	−0.02	0.02	−0.01	−0.09	0.17	1.00	
I^{Im}_{+-}	0.01	−0.06	0.01	−0.01	−0.04	0.01	0.01	1.00
I^{Re}_{+-}	0.02	−0.08	0.02	−0.04	−0.01	0.03	0.06	0.04
U^-_0	−0.04	0.01	−0.02	0.10	0.00	−0.05	−0.04	−0.00
U^+_0	−0.08	0.01	−0.02	0.01	−0.00	0.03	0.02	−0.00
$U^{-,\mathrm{Im}}_{-0}$	−0.05	−0.06	0.01	0.06	−0.01	0.05	0.09	0.01
$U^{-,\mathrm{Re}}_{-0}$	−0.03	0.02	−0.17	−0.01	−0.00	0.00	0.00	−0.01
$U^{+,\mathrm{Im}}_{-0}$	0.00	0.03	0.05	−0.05	0.01	−0.05	−0.09	−0.01
$U^{+,\mathrm{Re}}_{-0}$	0.03	−0.07	0.17	−0.11	−0.00	0.03	0.04	0.01
U^-_-	−0.00	−0.02	0.03	0.02	0.00	−0.01	−0.02	−0.00
U^+_-	−0.03	0.02	−0.07	0.06	−0.01	0.01	−0.01	0.00
$U^{-,\mathrm{Im}}_{+0}$	0.01	−0.00	−0.00	0.01	0.01	0.05	0.26	0.00
$U^{-,\mathrm{Re}}_{+0}$	−0.08	0.01	−0.01	0.01	−0.06	−0.06	−0.02	−0.00
$U^{+,\mathrm{Im}}_{+0}$	−0.01	−0.01	−0.00	0.01	−0.05	0.06	−0.01	−0.00
$U^{+,\mathrm{Re}}_{+0}$	0.05	−0.00	−0.00	0.01	−0.03	0.09	−0.09	−0.00
$U^{-,\mathrm{Im}}_{+-}$	0.01	−0.04	0.00	0.01	−0.04	0.01	0.03	0.04
$U^{-,\mathrm{Re}}_{+-}$	0.01	−0.01	0.00	−0.01	−0.00	0.01	0.01	−0.11
$U^{+,\mathrm{Im}}_{+-}$	0.02	−0.02	0.02	−0.03	−0.01	0.04	0.06	−0.04
$U^{+,\mathrm{Re}}_{+-}$	0.02	−0.04	0.02	−0.04	−0.03	0.04	0.08	0.08
U^-_+	0.01	−0.01	0.00	−0.01	−0.05	−0.03	−0.04	−0.00

TABLE XVI. (Continued from Table XV) Statistical correlation matrix for the U and I parameters. Elements above the diagonal are redundant and not included in the table. (Continued in Table XVII.)

	I^{Re}_{+-}	U^-_0	U^+_0	$U^{-,\mathrm{Im}}_{-0}$	$U^{-,\mathrm{Re}}_{-0}$	$U^{+,\mathrm{Im}}_{-0}$	$U^{+,\mathrm{Re}}_{-0}$	U^-_-	U^+_-
I^{Re}_{+-}	1.00								
U^-_0	−0.03	1.00							
U^+_0	−0.03	0.07	1.00						
$U^{-,\mathrm{Im}}_{-0}$	0.08	0.02	0.00	1.00					
$U^{-,\mathrm{Re}}_{-0}$	−0.02	−0.05	0.02	0.09	1.00				
$U^{+,\mathrm{Im}}_{-0}$	−0.09	0.02	0.05	−0.26	−0.04	1.00			
$U^{+,\mathrm{Re}}_{-0}$	0.06	−0.04	−0.07	0.06	0.01	−0.03	1.00		
U^-_-	0.01	0.00	−0.03	−0.08	−0.07	0.06	−0.02	1.00	
U^+_-	−0.05	0.05	0.26	0.02	0.05	−0.05	−0.05	−0.12	1.00
$U^{-,\mathrm{Im}}_{+0}$	0.01	0.13	0.05	0.02	−0.01	−0.01	−0.00	−0.01	0.01
$U^{-,\mathrm{Re}}_{+0}$	−0.02	−0.10	0.04	−0.03	0.02	0.03	−0.02	0.01	0.03
$U^{+,\mathrm{Im}}_{+0}$	−0.01	0.04	0.15	0.03	0.02	−0.01	−0.00	−0.01	0.07
$U^{+,\mathrm{Re}}_{+0}$	−0.01	0.02	−0.09	−0.00	0.01	−0.00	0.01	−0.00	0.02
$U^{-,\mathrm{Im}}_{+-}$	0.05	0.00	0.02	0.06	0.03	−0.05	0.01	0.01	0.06
$U^{-,\mathrm{Re}}_{+-}$	−0.04	−0.01	−0.01	0.02	0.00	−0.02	0.01	−0.08	−0.04
$U^{+,\mathrm{Im}}_{+-}$	0.01	−0.03	−0.01	0.12	0.01	−0.12	0.06	0.01	0.02
$U^{+,\mathrm{Re}}_{+-}$	0.14	−0.04	−0.03	0.11	−0.01	−0.12	0.07	−0.07	−0.06
U^-_+	0.04	−0.01	0.01	0.04	0.01	−0.04	0.01	−0.05	0.04

TABLE XVII. (Continued from Table XVI) Statistical correlation matrix for the U and I parameters. Elements above the diagonal are redundant and not included in the table.

	$U^{-,\mathrm{Im}}_{+0}$	$U^{-,\mathrm{Re}}_{+0}$	$U^{+,\mathrm{Im}}_{+0}$	$U^{+,\mathrm{Re}}_{+0}$	$U^{-,\mathrm{Im}}_{+-}$	$U^{-,\mathrm{Re}}_{+-}$	$U^{+,\mathrm{Im}}_{+-}$	$U^{+,\mathrm{Re}}_{+-}$	U^{-}_{+}
$U^{-,\mathrm{Im}}_{+0}$	1.00								
$U^{-,\mathrm{Re}}_{+0}$	−0.14	1.00							
$U^{+,\mathrm{Im}}_{+0}$	0.22	0.07	1.00						
$U^{+,\mathrm{Re}}_{+0}$	0.03	−0.01	−0.09	1.00					
$U^{-,\mathrm{Im}}_{+-}$	−0.00	0.00	0.03	0.00	1.00				
$U^{-,\mathrm{Re}}_{+-}$	0.00	−0.00	−0.00	−0.00	0.31	1.00			
$U^{+,\mathrm{Im}}_{+-}$	0.01	−0.02	0.02	−0.00	0.18	−0.06	1.00		
$U^{+,\mathrm{Re}}_{+-}$	0.01	−0.03	0.00	−0.00	−0.17	0.06	0.13	1.00	
U^{-}_{+}	0.04	−0.01	−0.00	0.02	−0.14	0.01	0.06	0.01	1.00

in the decay $B^0 \to \rho\pi$. The U and I parameters are related to the Q2B parameters through the relations of Eqs. (17)–(22).

We can also use the U and I parameters and associated correlations to extract the $B^0 \to \rho^0\pi^0$ CP-violation parameters and decay fraction,

$$\mathcal{C}_{00} = \frac{U^-_0}{U^+_0}, \tag{36}$$

$$\mathcal{S}_{00} = \frac{2I_0}{U^+_0}, \tag{37}$$

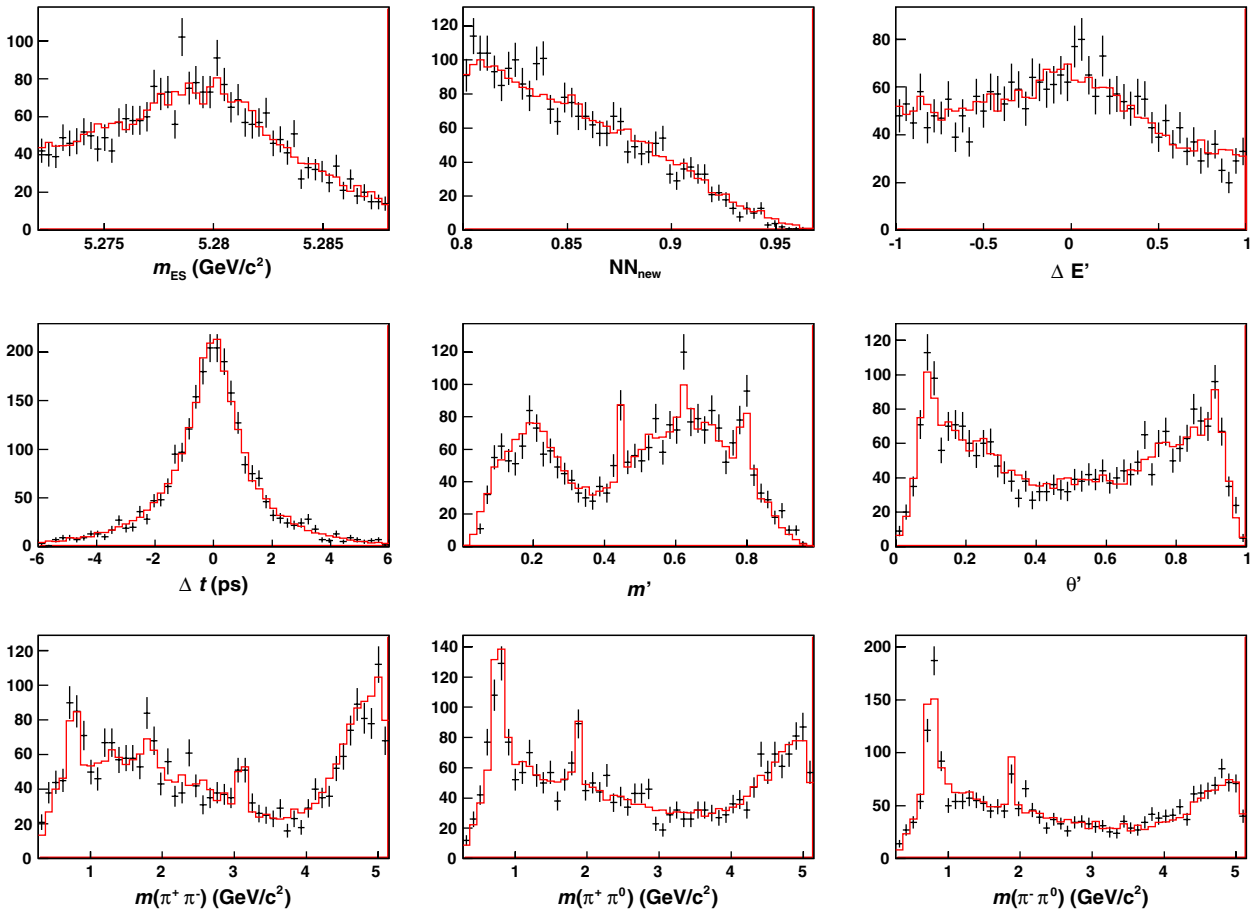

FIG. 6 (color online). Overlay plots of fit variable distributions in on-resonance data (points with error bars) and in a parametrized MC sample generated from the final fit results (red line) with 10 times the number of events in data. The MC histograms are scaled to have the same integral as the data histograms onto which they are overlaid. A restrictive selection criterion is applied to the NN output ($\mathrm{NN}_{\mathrm{new}} > 0.8$) to enhance the signal component.

$$f_{00} = \frac{U_0^+}{U_+^+ + U_-^+ + U_0^+}. \quad (38)$$

These eight Q2B parameters related to $\rho^\pm\pi^\mp$ and $\rho^0\pi^0$ decays are extracted using a χ^2 minimization technique that accounts for the statistical and systematic correlations between the U and I parameters. In each step of the minimization process, the current values of the free parameters are used to calculate the corresponding values of the eight U and I parameters on which they depend and a vector $V_{\rm diff}$ is constructed from the differences between these U and I parameter values and the values obtained in our final fit to the full on-resonance data set. The χ^2 is then calculated as

$$\chi^2_{\rm Q2B} = V^T_{\rm diff}(C^{\rm data})^{-1}V_{\rm diff}, \quad (39)$$

where $C^{\rm data}$ is the 8×8 covariance matrix for the relevant U and I parameters from the fit to data. Table XVIII presents the Q2B parameters extracted from the full fit to on-resonance data along with their statistical and systematic errors. In a study of correlations between $\sigma_{\Delta t}$ and DP position we find a small contribution to the systematic uncertainty on f_{00}, which is included in Table XVIII. The correlation matrix for the Q2B parameters is provided in Table XIX. A study of the Q2B parameters (see Appendix A 2) establishes that there is negligible bias in their extraction and good robustness in the presence of statistical fluctuations.

TABLE XVIII. Quasi-two-body parameter values and uncertainties corresponding to the fit to the complete on-resonance data set.

Param	Value	$\sigma_{\rm stat}$	$\sigma_{\rm syst}$
$\mathcal{A}_{\rho\pi}$	-0.100	0.029	0.021
$\mathcal{C}$	0.016	0.059	0.036
$\Delta\mathcal{C}$	0.234	0.061	0.048
$\mathcal{S}$	0.053	0.081	0.034
$\Delta\mathcal{S}$	0.054	0.082	0.039
$\mathcal{C}_{00}$	0.19	0.23	0.15
$\mathcal{S}_{00}$	-0.37	0.34	0.20
f_{00}	0.092	0.011	0.009

The parameters $\mathcal{A}_{\rho\pi}$ and $\mathcal{C}$ can be transformed into the direct *CP*-violation parameters $\mathcal{A}^{+-}_{\rho\pi}$ and $\mathcal{A}^{-+}_{\rho\pi}$ where

$$\mathcal{A}^{+-}_{\rho\pi} \equiv \frac{\Gamma(\bar{B}^0 \to \rho^-\pi^+) - \Gamma(B^0 \to \rho^+\pi^-)}{\Gamma(\bar{B}^0 \to \rho^-\pi^+) + \Gamma(B^0 \to \rho^+\pi^-)}, \quad (40)$$

$$\mathcal{A}^{-+}_{\rho\pi} \equiv \frac{\Gamma(\bar{B}^0 \to \rho^+\pi^-) - \Gamma(B^0 \to \rho^-\pi^+)}{\Gamma(\bar{B}^0 \to \rho^+\pi^-) + \Gamma(B^0 \to \rho^-\pi^+)}, \quad (41)$$

using the relations

$$\mathcal{A}^{+-}_{\rho\pi} = -\frac{\mathcal{A}_{\rho\pi} + \mathcal{C} + \mathcal{A}_{\rho\pi}\Delta\mathcal{C}}{1 + \Delta\mathcal{C} + \mathcal{A}_{\rho\pi}\mathcal{C}}, \quad (42)$$

$$\mathcal{A}^{-+}_{\rho\pi} = \frac{\mathcal{A}_{\rho\pi} - \mathcal{C} - \mathcal{A}_{\rho\pi}\Delta\mathcal{C}}{1 - \Delta\mathcal{C} - \mathcal{A}_{\rho\pi}\mathcal{C}}. \quad (43)$$

We extract the central values and uncertainties for these parameters using a χ^2 minimization procedure in the two-dimensional plane corresponding to $\mathcal{A}^{+-}_{\rho\pi}$ versus $\mathcal{A}^{-+}_{\rho\pi}$. At each point in the plane, the values of $\mathcal{A}^{+-}_{\rho\pi}$ and $\mathcal{A}^{-+}_{\rho\pi}$ are fixed and used in combination with $\Delta\mathcal{C}$ (which is free to vary) to determine the corresponding values of $\mathcal{A}_{\rho\pi}$ and $\mathcal{C}$. These values are then used in combination with $\Delta\mathcal{C}$ and the five other Q2B parameters to calculate a χ^2 value as described above. From this two-dimensional scan, we find

$$\mathcal{A}^{+-}_{\rho\pi} = 0.09^{+0.05}_{-0.06} \pm 0.04, \quad (44)$$

$$\mathcal{A}^{-+}_{\rho\pi} = -0.12 \pm 0.08^{+0.04}_{-0.05}, \quad (45)$$

with a correlation of 0.55 evaluated from the 1σ contour for statistical and systematic errors combined. A two-dimensional likelihood scan with combined statistical and systematic uncertainties and 68.3%, 95.5%, and 99.7% confidence-level contours is provided in Fig. 7. The origin, corresponding to no direct *CP* violation, lies on the 96.0% confidence-level contour ($\Delta\chi^2 = 6.42$), corresponding to a $p = 4.0\%$ probability, under the

TABLE XIX. Combined statistical and systematic correlation matrix for the quasi-two-body parameters corresponding to the fit to the complete on-resonance data set. Values above the diagonal are redundant and omitted for clarity.

	$\mathcal{A}_{\rho\pi}$	$\mathcal{C}$	$\Delta\mathcal{C}$	$\mathcal{S}$	$\Delta\mathcal{S}$	$\mathcal{C}_{00}$	$\mathcal{S}_{00}$	f_{00}
$\mathcal{A}_{\rho\pi}$	1.000							
$\mathcal{C}$	0.035	1.000						
$\Delta\mathcal{C}$	0.154	0.213	1.000					
$\mathcal{S}$	-0.040	-0.065	-0.070	1.000				
$\Delta\mathcal{S}$	-0.041	-0.038	-0.060	0.199	1.000			
$\mathcal{C}_{00}$	-0.088	-0.041	-0.034	0.026	0.011	1.000		
$\mathcal{S}_{00}$	-0.005	0.007	0.044	-0.081	-0.007	0.002	1.000	
f_{00}	0.074	0.009	0.016	0.029	-0.016	-0.062	0.062	1.000

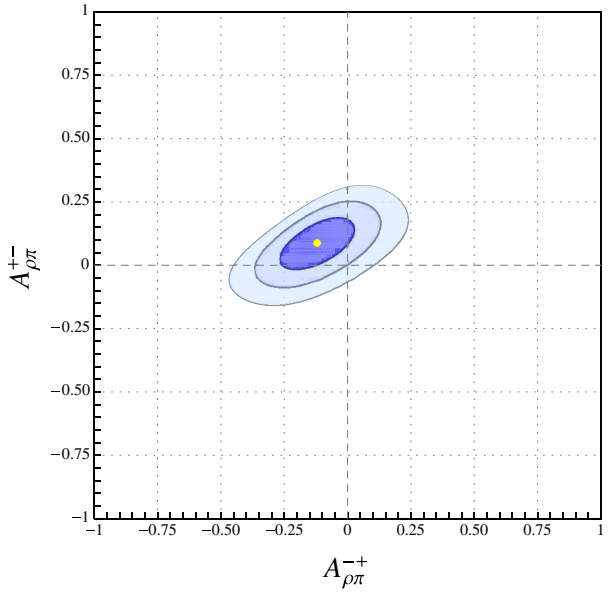

FIG. 7 (color online). Combined statistical and systematic two-dimensional likelihood scan of $\mathcal{A}^{+-}_{\rho\pi}$ versus $\mathcal{A}^{-+}_{\rho\pi}$ with 68.3%, 95.5%, and 99.7% confidence-level contours ($\Delta\chi^2 = \{2.30, 6.18, 11.83\}$). The yellow dot inside the contours indicates the central value.

assumption of no direct *CP* violation, of obtaining a result that deviates from the origin at least as much as ours.

B. Alpha scan

In order to extract likely values of α from the U and I parameters obtained in our final fit, we perform a scan of α from 0° to 180°. At each scan point, a χ^2-minimization fit is performed using the goodness of fit measure,

$$\chi^2(\alpha) = [V^{\text{data}} - V^{\text{scan}}]^T (C^{\text{data}})^{-1} [V^{\text{data}} - V^{\text{scan}}] + \left(\frac{1 - U_+^{+\text{scan}}}{\epsilon}\right)^2, \quad (46)$$

where C^{data} is the 26×26 covariance matrix for U s and I s from our fit to data and V^{data} and V^{scan} are vectors of the 26 U and I parameters from our fit to data and the current iteration of the minimization, respectively. The last term is a Gaussian constraint that restricts U_+^+ in the scan to lie within ϵ of 1 (the value to which it is fixed in the fits to data); ϵ is set to 0.0001. Because the overall scaling of the U and I parameters is not physically meaningful, U_+^+ is allowed to be exactly 1 in the fit and this constraint term does not significantly contribute to the total χ^2. In the χ^2-minimizations, the actual free parameters are the tree ($T^{\pm,0}$) and penguin ($P^{\pm}$) amplitudes, which are related to the ρ-resonance amplitudes through the formulas

$$A^+ = T^+ e^{-i\alpha} + P^+, \quad (47)$$

$$A^- = T^- e^{-i\alpha} + P^-, \quad (48)$$

$$A^0 = T^0 e^{-i\alpha} + P^0, \quad (49)$$

$$\bar{A}^+ = T^- e^{+i\alpha} + P^-, \quad (50)$$

$$\bar{A}^- = T^+ e^{+i\alpha} + P^+, \quad (51)$$

$$\bar{A}^0 = T^0 e^{+i\alpha} + P^0, \quad (52)$$

where

$$A^+ \equiv A(B^0 \to \rho^+ \pi^-), \quad (53)$$

$$A^- \equiv A(B^0 \to \rho^- \pi^+), \quad (54)$$

$$A^0 \equiv A(B^0 \to \rho^0 \pi^0), \quad (55)$$

$$\bar{A}^+ \equiv \frac{q}{p} A(\bar{B}^0 \to \rho^+ \pi^-), \quad (56)$$

$$\bar{A}^- \equiv \frac{q}{p} A(\bar{B}^0 \to \rho^- \pi^+), \quad (57)$$

$$\bar{A}^0 \equiv \frac{q}{p} A(\bar{B}^0 \to \rho^0 \pi^0). \quad (58)$$

Note that due to $SU(2)$ flavor symmetry, the third penguin amplitude can be calculated from the other two using the relation $P^0 = -\frac{1}{2}(P^+ + P^-)$ (see Refs. [20,21]). At each step in the minimization process, the current values of the tree and penguin amplitudes as well as the current fixed value of α are used to calculate the ρ-resonance amplitudes. These ρ amplitudes are then used to calculate the U and I parameters that comprise the vector V^{scan}, using Eqs. (12) through (16), which relate the U and I parameters to the ρ amplitudes. In the fits, we take advantage of a global phase that is not physically meaningful to fix the phase of T^+ to 0.

As the scan proceeds, a minimum χ^2 value is extracted from the fit at each value of α. We convert these χ^2 values to "Σ" values by calculating the χ^2 probability of each value according to

$$\Sigma \equiv \int_a^\infty f(x; 1) dx, \quad (59)$$

where a is the difference between the χ^2 at the current scan point and the minimum χ^2 for all the scan points, and $f(x; 1)$ is a χ^2 distribution with one degree of freedom. The variable "Σ" corresponds to what is commonly referred to as "1-Confidence Level" (1-C.L.) and is simply the p value of a χ^2 test at each scan point.

1. *Incorporating information from charged B decays*

Following the methods employed in Belle's 2007 $B^0 \to \rho\pi$ analysis [3] and described in Ref. [6], we perform a further α scan that makes use of measurements from the

charged decays $B^{\pm} \to \rho^{\pm,0}\pi^{0,\pm}$. Amplitudes for these modes can be related to amplitudes in the neutral B modes through isospin relations. These relations result in four "constraint" equations while introducing only two new free parameters in the fit (the real and imaginary parts of a tree amplitude, T^{+0}). The charged B measurements of interest are the following branching fractions and asymmetries:

$$\mathcal{B}(\rho^+\pi^0) = c(|A^{+0}|^2 + |A^{-0}|^2)\tau_{B^+}, \tag{60}$$

$$\mathcal{B}(\rho^0\pi^+) = c(|A^{0+}|^2 + |A^{0-}|^2)\tau_{B^+}, \tag{61}$$

$$\mathcal{A}(\rho^+\pi^0) = \frac{|A^{-0}|^2 - |A^{+0}|^2}{|A^{-0}|^2 + |A^{+0}|^2}, \tag{62}$$

$$\mathcal{A}(\rho^0\pi^+) = \frac{|A^{0-}|^2 - |A^{0+}|^2}{|A^{0-}|^2 + |A^{0+}|^2}, \tag{63}$$

where c is a constant and

$$A^{\pm 0} = \frac{q}{p}A(B^{\pm} \to \rho^{\pm}\pi^0), \tag{64}$$

$$A^{0\pm} = \frac{q}{p}A(B^{\pm} \to \rho^0\pi^{\pm}). \tag{65}$$

In the fit, we fix $c = 1$ and no longer require $U_+^+ = 1$. This is equivalent to letting c be a free parameter in the fit and setting $U_+^+ = 1$. Due to this convention, it is necessary to divide all the current values of the U and I parameters during the minimization process by the current value of U_+^+ before using them to calculate the current χ^2 value.

According to $SU(2)$ isospin symmetry, several relations hold between the amplitudes in Eqs. (53)–(58), (64), and (65),

$$A^+ + A^- + 2A^0 = e^{-2i\alpha}(\bar{A}^+ + \bar{A}^- + 2\bar{A}^0) \tag{66}$$

$$= \sqrt{2}(A^{+0} + A^{0+}) \tag{67}$$

$$= \sqrt{2}e^{-2i\alpha}(A^{-0} + A^{0-}), \tag{68}$$

$$A^{+0} - A^{0+} - \sqrt{2}(A^+ - A^-) = e^{-2i\alpha}[A^{-0} - A^{0-} - \sqrt{2}(A^- - A^+)]. \tag{69}$$

Based on these relations, we can parametrize the charged B amplitudes according to

$$\sqrt{2}A^{+0} = e^{-i\alpha}T^{+0} + P^+ - P^-, \tag{70}$$

$$\sqrt{2}A^{0+} = e^{-i\alpha}(T^+ + T^- + 2T^0 - T^{+0}) - P^+ + P^-, \tag{71}$$

$$\sqrt{2}A^{-0} = e^{+i\alpha}T^{+0} + P^+ - P^-, \tag{72}$$

$$\sqrt{2}A^{0-} = e^{+i\alpha}(T^+ + T^- + 2T^0 - T^{+0}) - P^+ + P^-. \tag{73}$$

When combined with Eqs. (47)–(52), which parametrize the neutral B amplitudes, this yields a parametrization that implicitly incorporates the isospin relations between the different charged and neutral B modes. Because the global phase is physically irrelevant, we fix it by requiring that $\mathrm{Im}T^+ = 0$.

The isospin "constrained" and "unconstrained" scans are performed identically, except that Eqs. (70)–(73) are included as Gaussian constraints in the χ^2 calculation. The system of equations (60)–(63) is used to express the magnitudes of $A^{\pm 0}$ and $A^{0\pm}$ in terms of the branching fractions and asymmetries for the charged B modes $B^{\pm} \to \rho^{\pm}\pi^0$ and $B^{\pm} \to \rho^0\pi^{\pm}$. Using world average measurements from [12], we calculate the value of each of these magnitudes as well as their uncertainties. At each step in the minimization process, and for each of Eqs. (70)–(73), a term is added to the χ^2,

$$\left(\frac{|A_{\mathrm{iter}}| - |A_{\mathrm{meas}}|}{\sigma_{|A_{\mathrm{meas}}|}}\right)^2, \tag{74}$$

where $|A_{\mathrm{iter}}|$ is the magnitude of the relevant $A^{\pm 0}$ or $A^{0\pm}$ parameter for the current iteration of the minimization process, $|A_{\mathrm{meas}}|$ is the magnitude of the amplitude based on branching fractions and asymmetry measurements, and $\sigma_{|A_{\mathrm{meas}}|}$ is the uncertainty in the value of the magnitude due to measurement uncertainties for the branching fractions and asymmetries. For those branching fractions and asymmetries that have asymmetric uncertainties, we choose whether to use the upper or lower error for the calculation in a given iteration by ascertaining whether the value of the branching fraction or asymmetry corresponding to the tree and penguin parameters in the current iteration of the minimization process is less than or greater than the experimental value, respectively.

2. Results of α scan

Plots of the χ^2 values from our final α scans with isospin constraints (solid red) and without isospin constraints (dashed black) are shown in Fig. 8. The corresponding Σ

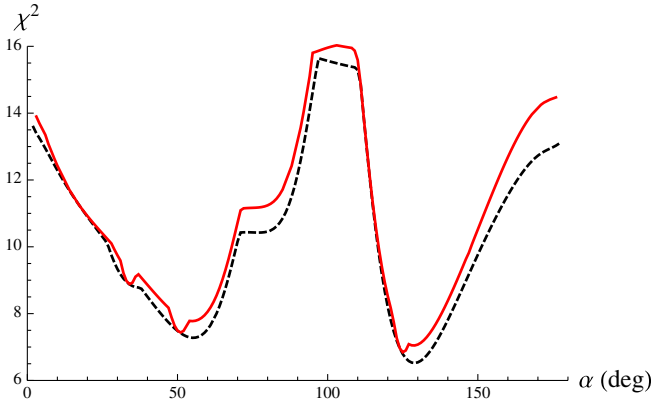

FIG. 8 (color online). Isospin-constrained (solid red) and unconstrained (dashed black) scans of minimum χ^2 values as a function of α. The scans are based on the fit to the full on-resonance data set and include contributions from both statistical and systematic uncertainties. Note that the origin is suppressed.

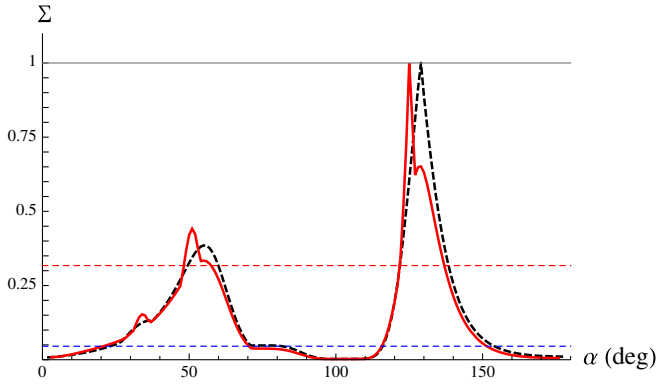

FIG. 9 (color online). Isospin-constrained (solid red) and unconstrained (dashed black) scans of Σ values as a function of α. The scans are based on the fit to the full on-resonance data set and include contributions from both statistical and systematic uncertainties. The upper and lower horizontal dashed lines correspond to $\Sigma = 0.05$ and 0.32, respectively.

distributions are presented in Fig. 9. As indicated by our robustness studies (see Appendix), the Σ scan is not robust and cannot be interpreted in terms of Gaussian statistics.

IX. CONCLUSION

We have performed a time-dependent Dalitz plot analysis of the mode $B^0 \to (\rho\pi)^0$ in which we extract 26 U and I parameter values describing the physics involved, as well as their full correlation matrix in an extended unbinned maximum likelihood fit. From these fit results, we extract the Q2B parameters $\mathcal{A}_{\rho\pi}$, $\mathcal{C}$, $\Delta\mathcal{C}$, $\mathcal{S}$, $\Delta\mathcal{S}$, $\mathcal{C}_{00}$, $\mathcal{S}_{00}$, and f_{00}, with values given in Table XVIII. These Q2B values are consistent with the results of the 2007 *BABAR* analysis [2] as well as the results obtained by the Belle Collaboration [3]. We also perform a two-dimensional likelihood scan of the direct CP-violation asymmetry parameters for $B^0 \to \rho^{\pm}\pi^{\mp}$ decays, finding the change in χ^2 between the minimum and the origin (corresponding to no direct CP-violation) to be $\Delta\chi^2 = 6.42$. Finally, we perform one-dimensional likelihood scans of the unitarity angle α (see Fig. 8) both with (solid red) and without (dashed black) isospin constraints. However, as indicated by our robustness studies (Appendix A 3), the extraction of α with our current sample size is not robust. Maximum likelihood estimators are known to be Gaussian in general only in the limit of large data sets. Our studies indicate that other currently published measurements of α from $B^0 \to \rho\pi$ decays suffer from a similar lack of robustness. This analysis would benefit greatly from increased sample sizes.

ACKNOWLEDGMENTS

We are grateful for the extraordinary contributions of our PEP-II colleagues in achieving the excellent luminosity and machine conditions that have made this work possible. The success of this project also relies critically on the expertise and dedication of the computing organizations that support *BABAR*. The collaborating institutions wish to thank SLAC for its support and the kind hospitality extended to them. This work is supported by the U.S. Department of Energy and National Science Foundation, the Natural Sciences and Engineering Research Council (Canada), the Commissariat à l'Energie Atomique and Institut National de Physique Nucléaire et de Physique des Particules (France), the Bundesministerium für Bildung und Forschung and Deutsche Forschungsgemeinschaft (Germany), the Istituto Nazionale di Fisica Nucleare (Italy), the Foundation for Fundamental Research on Matter (The Netherlands), the Research Council of Norway, the Ministry of Education and Science of the Russian Federation, Ministerio de Ciencia e Innovación (Spain), and the Science and Technology Facilities Council (United Kingdom). Individuals have received support from the Marie-Curie IEF program (European Union) and the A. P. Sloan Foundation (USA).

APPENDIX A: ROBUSTNESS STUDIES

We assess the robustness with which the fit framework extracts statistically accurate values and uncertainties for the U and I parameters, the Q2B parameters, and α, by employing MC-simulated samples generated with a parametrized detector simulation and with signal and background contributions corresponding to those expected in the full on-resonance data set. The simulated samples are generated using physical U and I parameters based on specific tree and penguin amplitudes and $\alpha = 89°$ (approximately the world average). Each simulated dataset is generated with the same parameter values, but a different random-number seed. By examining the results of the fits to each of these simulated datasets, we assess the fit robustness.

For these studies, we use 25 samples generated with different seeds, so that the uncertainty on the bias is negligible compared to the other uncertainties.

1. U and I parameter robustness studies

For each of the 26 U and I parameters extracted in the fits to the MC samples, we calculate the RMS (across the 25 MC samples) of the differences (measured in units of the statistical uncertainty on the extracted values of the parameters) between the generated and extracted values of the parameters. We also calculate the average across the 25 MC samples of these differences for each of the U and I parameters. The RMS difference, averaged across the 26 U and I parameters, is 1.17, while the difference in units of statistical uncertainty, averaged across the U and I parameters, is 0.04. This demonstrates that the U and I parameter values are extracted robustly and with negligible bias.

2. Quasi-two-body robustness studies

The results of the robustness study of the Q2B parameters are provided in Table XX. In this table, the first column

TABLE XX. Results of robustness study of quasi-two-body parameters. The first column of numbers is the ratio of the square root of the variance divided by the mean error on the fit to the parameter across 25 MC samples. The second column is the average difference (measured in units of statistical uncertainty, σ, on the extracted values of the parameters) between the extracted value of the parameter and its generated value, across all MC samples. The third column is the same as the second, except that the absolute value of each difference is taken before averaging.

Param	$\sqrt{\text{Variance}}/\langle\sigma\rangle$	Avg #σ Diff From Gen Val	Avg Abs #σ Diff From Gen Val
$\mathcal{A}_{\rho\pi}$	0.94	−0.13	0.76
$\mathcal{C}$	1.15	0.06	0.90
$\Delta\mathcal{C}$	0.94	0.04	0.75
$\mathcal{S}$	1.11	0.03	0.92
$\Delta\mathcal{S}$	1.02	−0.20	0.82
$\mathcal{C}_{00}$	1.15	−0.10	0.89
$\mathcal{S}_{00}$	1.13	0.23	0.92
f_{00}	1.08	0.28	0.93

of numbers is the ratio of the square root of the variance of the parameter across 25 MC samples divided by the mean error on the fit to the parameter across all MC samples. As one would expect, the square root of the variance of each parameter value is approximately equal to the mean statistical uncertainty on the variable as extracted from the fits to MC samples. The second column is the average difference (measured in units of statistical uncertainty, σ, on the extracted values of the parameters) between the extracted value of the parameter and its generated value, across all MC samples. These values are all within 0.28σ of 0, indicating negligible bias. The third column is the same as the second, except that the absolute value of each difference is taken before averaging. These values are no greater than 0.93σ, indicating that the extracted values of the parameters are reliably close to the generated values. Taken together, these results indicate that the extraction of the Q2B parameters is robust to possible non-Gaussian fluctuations, and unbiased.

3. α robustness studies

The results of the robustness scans of α are provided in Table XXI, sorted by the absolute difference between the extracted α-scan peak position and the generated value of 89°. The first column lists the position of the most favored value of α in the scan. The second and third columns list the upper and lower errors, respectively, which are calculated as the number of degrees to either side of the α scan peak position at which the Σ value drops to 0.32. The fourth column lists the mean of the upper and lower errors while the fifth column lists the value of the minimum χ^2 obtained at the α scan peak position. The second to last

TABLE XXI. Results of parametrized MC study of robustness of α scans. The generated value α is $\alpha_{\text{gen}} = 89°$ and the columns are described in the text.

α Scan Peak	Upper Error	Lower Error	Mean Error	Min χ^2	$\sqrt{2\Delta\chi^2}$ Dist From $\chi^2(\alpha_{\text{gen}})$	#σ Between Gen and Fit Peaks
43	+5	−4	5	27.2	2.6	−9.0
44	+5	−5	5	18.7	5.3	−8.5
48	+5	−5	5	21.0	2.3	−8.2
49	+5	−5	5	24.2	2.9	−8.7
52	+5	−5	5	16.1	2.4	−8.2
53	+5	−21	13	23.2	1.5	−7.2
60	+14	−8	11	16.5	3.3	−2.1
74	+7	−6	7	21.2	0.7	−2.1
74	+5	−13	9	15.9	4.1	−2.9
75	+10	−8	9	21.3	1.8	−1.5
76	+8	−18	13	21.3	2.5	−1.7
80	+5	−6	6	30.0	2.3	−1.7
83	+6	−7	7	24.0	1.3	−0.9
84	+6	−6	6	26.4	1.3	−0.9
84	+7	−6	7	30.1	1.0	−0.7
87	+7	−7	7	22.9	0.4	−0.3
88	+7	−6	7	10.9	0.1	−0.1
89	+9	−8	8	23.4	0.00	0
91	+9	−9	9	33.1	0.3	0.2
91	+4	−5	5	63.3	0.6	0.4
92	+8	−6	7	39.2	0.7	0.5
94	+7	−6	6	10.0	1.3	0.9
112	+5	−6	5	19.0	3.0	3.9
115	+5	−6	5	23.3	2.2	4.6
124	+28	−15	22	25.6	1.4	2.3

column gives a measure of the consistency between the likelihoods for the peak α position and the generated α position based on the change in χ^2, and the last column is the distance in σ between the generated and extracted α peak positions (where the upper or lower error is used as appropriate). For 17 of the 25 scans, the extracted value of α lies within 3σ of the generated value. Examining the individual α scans reveals three distinct solutions for α that tend to be favored (including the generated value of 89°) and each scan tends to include at least one secondary peak in addition to the primary peak. Figure 10 illustrates the three solutions for alpha by providing the sum of 25 normalized Gaussians with means and widths determined by the peak positions and symmetric errors extracted from the 25α scans. Also plotted are the individual Gaussians that contribute to the total PDF. Because the errors are not truly Gaussian, Fig. 10 provides an incomplete picture of the scan results. A better illustration is provided by Fig. 11, which displays the total Σ distribution obtained by summing all 25 Σ α scans after normalizing each to the same area. The total distribution is scaled so that it peaks at 1.

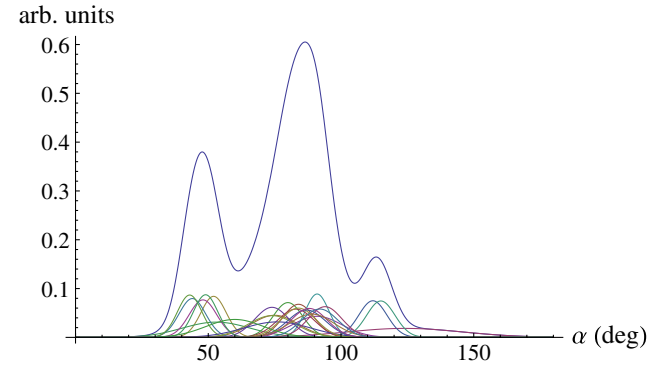

FIG. 10 (color online). Plot of the sum of 25 normalized Gaussians with means and widths determined by the peak positions and mean errors extracted from the 25α scans of parametrized MC generated with $\alpha = 89°$. Also plotted are the individual Gaussians that contribute to the total PDF.

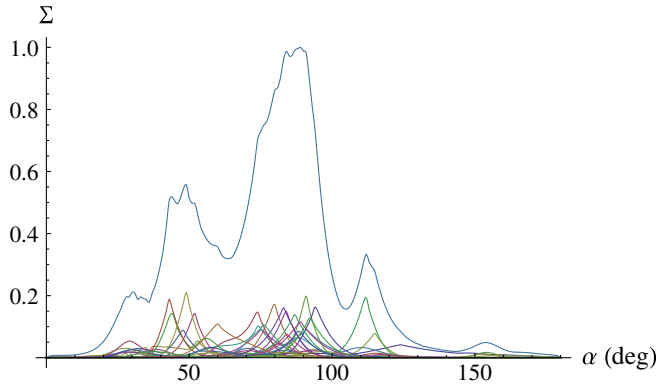

FIG. 11 (color online). Plot of the total Σ distribution obtained by summing all 25 Σ α scans of parametrized MC generated with $\alpha = 89°$ after normalizing their areas to 1. The total distribution is scaled so that it peaks at 1. Also plotted are the individual scaled Σ scans that contribute to the total distribution.

Also plotted are the individual scaled Σ scans that contribute to the total distribution. The final PDF closely resembles that obtained by naively summing Gaussian distributions, though it exhibits more fine features. Again, the distribution indicates three distinct solutions for α, with the generated value of 89° being favored. At the 1σ level ($\Sigma = 0.32$), the total scan distribution allows both the central and left peak. The presence of these secondary solutions indicates that with the current signal sample size and background levels, there is still a significant possibility that the favored value of α in a particular scan will correspond to a secondary solution.

[1] Throughout this paper, whenever a mode is given, the charge conjugate is also implied unless indicated otherwise.
[2] B. Aubert *et al.* (*BABAR* Collaboration), Phys. Rev. D **76**, 012004 (2007).
[3] A. Kusaka *et al.* (Belle Collaboration), Phys. Rev. D **77**, 072001 (2008).
[4] H. R. Quinn and A. E. Snyder, Phys. Rev. D **48**, 2139 (1993).
[5] G. J. Gounaris and J. J. Sakurai, Phys. Rev. Lett. **21**, 244 (1968).
[6] H. R. Quinn and J. P. Silva, Phys. Rev. D **62**, 054002 (2000).
[7] B. Aubert *et al.* (*BABAR* Collaboration), Phys. Rev. Lett. **91**, 201802 (2003).
[8] B. Aubert *et al.* (*BABAR* Collaboration), Nucl. Instrum. Methods Phys. Res., Sect. A **479**, 1 (2002).
[9] J. P. Lees *et al.* (*BABAR* Collaboration), arXiv:1301.2703.
[10] S. Agostinelli *et al.* (GEANT4 Collaboration), Nucl. Instrum. Methods Phys. Res., Sect. A **506**, 250 (2003).
[11] J. Beringer *et al.* (Particle Data Group), Phys. Rev. D **86**, 010001 (2012).
[12] K. Nakamura *et al.* (Particle Data Group), J. Phys. G **37**, 075021 (2010).
[13] A. Hoecker *et al.*, "TMVA toolkit for multivariate data analysis with root," http://tmva.sourceforge.net/.
[14] B. Aubert *et al.* (*BABAR* Collaboration), Phys. Rev. D **79**, 072009 (2009).
[15] H. Albrecht *et al.*, Z. Phys. C **48**, 543 (1990).
[16] B. Efron, *The Jackknife, the Bootstrap and Other Resampling Plans* (Society for Industrial and Applied Mathematics, Philadelphia, 1987).
[17] R. Barate *et al.* (ALEPH Collaboration), Z. Phys. C **76**, 15 (1997).
[18] R. R. Akhmetshin *et al.* (CMD-2 Collaboration), Phys. Lett. B **527**, 161 (2002).
[19] S. Schael *et al.* (ALEPH Collaboration), Phys. Rep. **421**, 191 (2005).
[20] H. J. Lipkin, Y. Nir, H. R. Quinn, and A. Snyder, Phys. Rev. D **44**, 1454 (1991).
[21] I. Dunietz, H. R. Quinn, A. Snyder, W. Toki, and H. J. Lipkin, Phys. Rev. D **43**, 2193 (1991).